2021

The Importance of Organic Content to Fractal Floc Properties in Estuarine Surface Waters: Insights From Video, LISST, and Pump Sampling

Kelsey A. Fall
Virginia Institute of Marine Science

Carl T. Friedrichs
Virginia Institute of Marine Science

Grace M. Massey
Virginia Institute of Marine Science

David G. Bowers

S. Jarrell Smith

Recommended Citation

Fall, Kelsey A.; Friedrichs, Carl T.; Massey, Grace M.; Bowers, David G.; and Smith, S. Jarrell, The Importance of Organic Content to Fractal Floc Properties in Estuarine Surface Waters: Insights From Video, LISST, and Pump Sampling (2021). *JGR Oceans*, 126, e2020JC016787.
doi: 10.1029/2020JC016787

JGR Oceans

RESEARCH ARTICLE
10.1029/2020JC016787

Key Points:

- A new method to solve the multiple floc fractal properties by combining laser diffraction, video settling, and pump sampling is presented
- Organic matter content is an important control on the size and density of primary particles and on the apparent density of microflocs
- The fractal dimension of microflocs is found to vary less than the primary particle size or primary particle density

Correspondence to:
K. A. Fall,
Kelsey.A.Fall@usace.army.mil

Citation:
Fall, K. A., Friedrichs, C. T., Massey, G. M., Bowers, D. G., & Smith, S. J. (2021). The importance of organic content to fractal floc properties in estuarine surface waters: Insights from video, LISST, and pump sampling. *Journal of Geophysical Research: Oceans*, *126*, e2020JC016787. https://doi.org/10.1029/2020JC016787

Received 10 SEP 2020
Accepted 20 NOV 2020

The Importance of Organic Content to Fractal Floc Properties in Estuarine Surface Waters: Insights From Video, LISST, and Pump Sampling

Kelsey A. Fall[1,2], Carl T. Friedrichs[1], Grace M. Massey[1], David G. Bowers[3], and S. Jarrell Smith[1]

[1]Virginia Institute of Marine Science, William & Mary, Gloucester Point, VA, USA, [2]U.S. Army Engineer Research and Development Center, Vicksburg, MS, USA, [3]School of Ocean Sciences, Bangor University, Bangor, Gwynedd, UK

Abstract To better understand the nature of flocs of varying organic content in estuarine surface waters, Laser in situ Scattering and Transmissometry, video settling, and pump sampling were deployed in the York River estuary. A new in situ method was developed to simultaneously solve the floc fractal dimension (F), primary particle size (d_p), and primary particle density (ρ_p) by fitting a simple fractal model to observations of effective floc density ($\Delta\rho$) as a function of floc diameter (d_f), while ensuring that the integrated particle size distribution was consistent with measurements of bulk apparent density (ρ_a). When fractal fits were statistically justified, application of the above methods showed the bulk fraction of organic matter (f_{org}) to be well correlated to multiple floc properties. As f_{org} increased, d_p and ρ_a also increased, while ρ_p, total suspended solids (TSS), and median floc size decreased. Notably for microflocs, neither F nor $\Delta\rho$ was significantly related to either f_{org} or TSS. This indicates that organic matter may partially displace water content within microflocs without fundamentally changing the flocs' inorganic structure. When pooling multiple samples, a marked decrease in F was seen at the transition to macroflocs, and most strongly for high f_{org} cases. This suggested that settling velocities $\geq \sim$1 mm/s may produce turbulent stresses that tend to tear macroflocs apart. This study also found that when the fractal theory held, ρ_p had a near 1:1 correlation with the bulk dry density of filtered TSS, implying that primary particles are tightly bound aggregates of combined mineral and organic components.

Plain Language Summary Particles suspended near the surface in estuaries are especially important for estuarine ecology and water quality management, because they can decrease the water clarity by scattering and absorbing the incoming light. Typically, these estuarine particles are not single solid mineral grains, but instead are clusters of inorganic and organic particles and water, called flocs. This study combined observations from water sampling, advanced optical instrumentation, and an in situ video camera to investigate the size, density, and composition of flocs suspended near the surface. It was found that simple mathematical relationships could be applied to describe the key properties of near-surface flocs, and that the relative amount of organic matter was an important control on the floc characteristics.

1. Introduction

The properties of particles in surface waters are especially important for the fate of incident light, with direct ramifications for primary production, habitat and water quality, and optical remote sensing. The rate of absorption and scattering of light depends directly on the particle size, composition, and density (Bowers et al., 2011) and indirectly on the particle settling rate, which controls how long and how high in the water column particles remain in suspension (Friedrichs et al., 2008). In the York River estuary and the adjacent Chesapeake Bay, the period of 1985–2016 was marked by a significant long-term decrease in water clarity as measured by the Secchi depth (Murphy et al., 2019). Gallegos et al. (2011) showed via optical modeling that the systematic decrease in Secchi depth in the Chesapeake Bay since the 1980s was likely due to an increase in the abundance of small, organic-rich suspended particles in the estuarine surface waters. The study of the York River estuary presented in the present paper was motivated in large part by a need to better understand the effects of organic matter content on the properties of particles in surface water due to the key role of organic-rich suspensions in affecting the water clarity in estuarine environments.

Typical near-surface estuarine particles are not single solid particles, but clusters of inorganic and organic particles and water, called flocs. Due to the fragile nature of flocs, in situ sampling is required to accurately characterize the optically important characteristics, including floc size (d_f), floc density (ρ_f), and floc settling velocity (w_s). When possible, an attractive way in which to represent the variation of ρ_f and w_s as a function of d_f is through fractal relationships. Kranenburg (1994) used the fractal approach to establish a mathematical relationship to relate d_f, ρ_f, and w_s to the diameter (d_p) and density (ρ_p) of the fractal primary particles using a dimensionless parameter, defined as the fractal dimension (F). The parameters d_p and ρ_p are difficult to measure for natural suspensions (Fettweis, 2008). Fortunately, if a video imaging system equipped with a settling column is available, F can be derived by fitting a power-law function to observed d_f and w_s or (via theoretical or empirical settling laws, e.g., Maggi, 2013; Soulsby, 1997) to d_f and ρ_f, simplified as $\rho_f \sim d_f^{3-F}$ (Dyer & Manning, 1999; Sanford et al., 2005; Smith & Friedrichs, 2015).

The fractal nature of flocs in estuarine surface waters is not well understood, in large part due to the challenges associated with collecting in situ observations of floc properties of surface suspensions. Relative to near-bed in situ observations, these challenges include the motion of observing platforms, lower particle concentrations, smaller particles, lower settling velocities, and lower contrast in optical imaging. Video settling systems and particle imaging cameras generally have limited size resolution, most requiring particles to be at least three pixels or larger for accurate tracking for d_f and w_s (Mikkelsen et al., 2004; Milligan & Hill, 1998; Sanford et al., 2005; Smith & Friedrichs, 2011). In addition, video settling systems generally require a stable platform to help ensure that estimates of w_s are not influenced by background fluid velocity, although Smith and Friedrichs (2011, 2015) have developed an automated method for reducing the background fluid effect. Otherwise, the time required to allow turbulence to completely dissipate and/or transfer water samples to a ship or shore-based laboratory may cause the flocs to evolve away from in situ conditions (Dyer et al., 1996). Particles in low-concentration surface waters in estuarine and coastal environments also tend to contain a relatively large fraction of organic matter, so fractal models inferred from the analysis of mainly inorganic flocs may not be appropriate in such cases (Braithwaite et al., 2010; Hill et al., 2011; Winterwerp & van Kesteren, 2004).

Diverse mathematical models have been developed to evaluate floc dynamics in coastal systems, and many of them depend on the underlying fractal formulations (e.g., Khelifa & Hill, 2006; Lee et al., 2014; Maggi, 2007; Son & Hsu, 2011; Verney et al., 2011; Winterwerp, 2002, 1998). These models vary in complexity and ability, but they all assume a fractal approach and require inputs of F, d_p, and ρ_p. It is common to set ρ_p near that of quartz or clay and d_p as 1, 4, or 10 μm (Dyer & Manning, 1999; Hurley et al., 2016; Sanford et al., 2005; Son & Hsu, 2011; Verney et al., 2011; Winterwerp, 1998), although the density of ρ_p may be significantly less than the commonly assumed inorganic value of ~2,600 kg/m^3 (Fettweis, 2008; Khelifa & Hill, 2006). These parameters can also be treated as adjustable fitting parameters (Lee et al., 2014). F is either assumed to be constant (Son & Hsu, 2011; Verney et al., 2011; Winterwerp, 1998) or to vary with floc size (Khelifa & Hill, 2006; Maggi, 2013; Son & Hsu, 2011). Son and Hsu (2011) compared simulations that used a constant F to simulations using size-varying F, and they found that the size-varying F better captured the essential features of cohesive sediment transport in the Ems/Dollar estuary. Verney et al. (2011) also compared F assumptions, as well as the influence of d_p, and found that a small variability in F did not have nearly as significant an effect on the results as did changes in d_p. The importance of d_p and ρ_p is also suggested in Khelifa and Hill (2006) and Fettweis (2008). Both note that the main uncertainties in the fractal approximations of floc ρ_f and w_s are associated with the characterization of d_p and ρ_p.

A fractal model, such as Kranenburg's (1994) floc density relationship, along with observations of total suspended solids (TSS) and the integration of an observed particle size distribution (PSD), can be used to constrain relationships between F, d_p, and ρ_p (Bowers, et al., 2017; Braithwaite et al., 2010; Chapalain et al., 2018; Ganju et al., 2007). Typically, constant values for d_p and ρ_p are assumed, and a best-fit solution for F is obtained for a given PSD. If multiple PSDs are fit at once, then a best-fit value for d_p, ρ_p, and F can be solved for simultaneously, which together minimize error across all the PSDs (Braithwaite et al., 2010). Braithwaite et al. (2010) used the above approach to define a representative d_p and ρ_p for the Tamar Estuary, and then used those values to estimate F throughout the system. They concluded that the relationship was fairly robust and useful for predicting single characteristic values for d_p and ρ_p for multiple PSDs and TSS samples. Bowers et al. (2017) and Chapalain et al. (2018) assumed a constant ρ_p and d_p across multiple PSDs and then determined the best-fit values for F for each sample separately.

Excess density ($\Delta\rho$) and apparent density (ρ_a) are two related definitions of particle density that are each commonly utilized when characterizing floc properties. Both have been used in the applications described above. Excess density, which is a floc's wet density minus the density of water, appears in particle settling relationships that balance a particle's effective submerged weight against frictional drag as a particle settles. Video settling tubes are often used to estimate $\Delta\rho$ through direct measurements of particle size and settling velocity (e.g., Dyer & Manning, 1999; Fennessy & Dyer, 1996; Hill et al., 1998; Mikkelsen et al., 2004; Smith & Friedrichs, 2011, 2015; Van Leussen & Cornelisse, 1993). In contrast, apparent density (ρ_a) is a floc's dry mass divided by its wet volume. Typically, measurements of dry mass concentration determined by filtration, combined with estimates of total wet floc volume, provide bulk estimates of ρ_a (e.g., Bowers et al., 2009, 2011; Braithwaite et al., 2010; Hurley et al., 2016; Mikkelsen & Pejrup, 2001). If one assumes that flocs are aggregates composed of interstitial water combined with primary particles of uniform density (which contain no water), then it is relatively straightforward to derive a quantitative relationship between $\Delta\rho$ and ρ_a, which can be used to determine the fractal characteristics.

Although previous measurements of $\Delta\rho$ or ρ_a have been shown to be useful for quantifying the fractal and primary particle characteristics (Bowers et al., 2017; Braithwaite et al., 2010; Chapalain et al., 2018; Ganju et al., 2007), the approaches applied to date have still been somewhat constrained, since varying values for d_p and ρ_p from sample to sample have not been considered. The work in this present study demonstrates a new method to characterize ρ_p, d_p, and F simultaneously for a single PSD by simultaneously including observations from both a video settling tube and a Laser in situ Scattering and Transmissometry (LISST). Observations from the video settling tube allow for well-constrained estimates of F along with unique estimates of ρ_p and d_p for each PSD. Independent measurements of ρ_p through analysis of the organic fraction of each collected water sample provide validation of the fractal assumption. These improvements allow us to gain new insight into the fractal nature of small, organic-rich flocs in estuarine surface waters.

In the sections that follow, we first outline the theoretical relationship between floc excess density ($\Delta\rho$) and apparent density (ρ_a) and how the relationship can be used with fractal approximations to determine d_p and ρ_p (Section 2). Next a description of specific instrumentation and analysis methods is provided (Section 3). In the results section (Section 4), both bulk floc characteristics and fractal properties are described, with special attention to trends correlated to floc organic content. The discussion (Section 5) focuses on how the results impact our previous understanding of fractal floc properties and their relationship to environmental conditions. Finally, the paper ends with conclusions and recommended future work (section 6). A list of symbols used in this paper is contained in Table 1.

2. Theoretical Background

2.1. Relationships Among $\Delta\rho$, ρ_a, and Primary Particle Density (ρ_p)

The quantitative relationship between $\Delta\rho$ and ρ_a follows from the definition of each, re-expressed in terms of the masses and volumes of the component particles and interstitial water (Fettweis, 2008; Hurley et al., 2016; Mikkelsen & Pejrup, 2001). A floc's wet density (ρ_f) can be described as the wet mass of the floc (M_f) divided by the volume of the floc (V_f), where M_f is the sum of the mass of the primary particles (M_p) and water (M_w) within the floc, and V_f is the sum of the volume of the primary particles (V_p) and water (V_w). Using these definitions and some algebra, it follows that

$$\Delta\rho = \rho_f - \rho_w = \frac{M_p + M_w}{V_p + V_w} - \frac{M_w}{V_w} = \frac{V_w M_p - V_p M_w}{\left(V_p + V_w\right)V_w} \tag{1}$$

where $\rho_w = M_w/V_w$ is the density of water. A floc's apparent density (ρ_a) is simply M_p/V_f, which can be expanded as

$$\rho_a = \frac{M_p}{V_p + V_w} \tag{2}$$

Dividing Equation 1 by 2 then yields

Table 1
Description of Symbol Notations Used in This Paper

Symbol	Meaning	Units
α	Scaling factor for PICS volume concentration	
$\Delta\rho$	Floc excess density (flocs's wet density minus the density of water)	kg/m^3
$\Delta\rho_{200\mu m}$	Average excess density for 200 μm macroflocs	kg/m^3
$\Delta\rho_{60\mu m}$	Average excess density for 60 μm microflocs	kg/m^3
ρ_a	Floc apparent density (floc's dry mass divided by its wet volume)	kg/m^3
$\rho_{a\_200\mu m}$	Average apparent density for 200 μm macroflocs	kg/m^3
$\rho_{a\_60\mu m}$	Average apparent density for 60 μm microflocs	kg/m^3
ρ_{a_bulk}	Bulk apparent density, determined from PSD total volume concentration divided by pump TSS	kg/m^3
ρ_f	Floc wet density	kg/m^3
ρ_{org}/ρ_{inorg}	Density of organic, inorganic solids	kg/m^3
ρ_p	Primary particle density	kg/m^3
ρ_{tss}	Primary particle density inferred from *TSS* and f_{org} (Equation 10)	kg/m^3
ρ_w	Density of water	kg/m^3
υ	Kinematic viscosity	m^2/s^1
d_f	Floc diameter	μm
d_p	Primary particle diameter	μm
d_{50v}	Median grain size by volume	μm
F	Fractal dimension	
F_{bulk}	Bulk fractal dimension inferred from the power law between PSD $d50v$ and ρ_{a_bulk}	
F_{macro}	Fractal dimension fit from PICS for macroflocs	
F_{micro}	Fractal dimension fit from PICS for microflocs	
f_{org}	Fraction organic by mass estimated by loss on ignition	
g	Gravitational acceleration, ~9.8	m/s^2
i	Size class bin i	
M_f	Total floc wet mass	kg
M_p	Total mass of primary particles (solids) within a floc	kg
M_w	Total mass of water within a floc	kg
PSD	Particle size distribution	μL/L
S	Salinity	ppt
U	Current speed	cm/s
TSS	Total suspended solids (in mass concentration) from pump samples	mg/L
TSS_F	Fractal estimated mass concentration from PSDs	mg/L
VC_i	Volume concentration in size class bin i	μL/L
$VC_{LISSSTi}$	LISST-100X volume concentration in size class bin i	μL/L
VC_{PICSi}	PICS volume concentration in size class bin i	mm^3
V_f	Total floc volume	m^3
V_p	Total volume of primary particles (solids) within a floc	m^3
V_s	Total sample volume	L
V_w	Total volume of water within a floc	m^3
w_s	Floc settling velocity	mm/s

Abbreviations: LISST, Laser in situ Scattering and Transmissometry; PICS, particle imaging camera system; PSD, particle size distribution; TSS, total suspended solids.

$$\frac{\Delta\rho}{\rho_a} = \frac{V_w M_p - V_p M_w}{V_w M_p} = 1 - \frac{\rho_w}{\rho_p} \tag{3}$$

where $\rho_p = M_p/V_p$ is the primary particle density. From Equation 3, it is evident that the ratio of excess density to apparent density is a function of primary particle density. For a given floc population, this ratio will remain constant across all floc sizes and floc densities if the density of the primary particles is uniform within that population.

Based on the relationships outlined above, concurrent, independent measurements of ρ_a and $\Delta\rho$ together can be used to estimate the ρ_p for a given floc population. If independent observations of $\Delta\rho$ and ρ_a confirm a stable ratio between $\Delta\rho$ and ρ_a across a range of floc sizes, then that ratio can be used to directly estimate ρ_p via Equation 3. This method for estimating ρ_p does not require any assumptions regarding the fractal nature of the flocculation process, nor does it assume that the primary particles are of a single size. It only assumes that the densities of the primary particles are uniform within a given floc. Unfortunately, obtaining independent in situ measurements of both ρ_a and $\Delta\rho$ for individual flocs is quite difficult. Advances in video settling tubes have made it easier to obtain measurements of $\Delta\rho$ for individual flocs, but often the best that can be done to obtain a second independent measurement of ρ_a is to measure a bulk or average value.

2.2. Use of Fractal Relationship Between $\Delta\rho$ and ρ_a to Estimate ρ_p and d_p

The constant ratio between $\Delta\rho$ and ρ_a derived above also means that for flocs that do conform to classical fractal relations, the same fractal dimension will describe the dependence of both $\Delta\rho$ and ρ_a on the floc size. Self-similar fractal theory was originally applied to $\Delta\rho$ by Kranenburg (1994), yielding

$$\Delta\rho = \rho_f - \rho_w = \left(\rho_p - \rho_w\right)\left[\frac{d_p}{d_f}\right]^{3-F} \tag{4}$$

where d_p and d_f are the primary particle and floc diameters, and F is the floc fractal dimension. In deriving Equation 4, Kranenburg (1994) assumed that primary particles in a given fractal floc population are of a single size, d_p, as well as a single density, ρ_p, and yield a specific excess density ($\Delta\rho$) for a corresponding floc size (d_f). Using Equation 3 to eliminate $\Delta\rho$ in Equation 4 immediately yields

$$\rho_a = \rho_p\left[\frac{d_p}{d_f}\right]^{3-F} \tag{5}$$

that is, the same fractal relation in terms of apparent density. The above results are consistent with the approach of other authors who have previously assumed that either $\Delta\rho$ (Dyer & Manning, 1999; Fettweis, 2008; Hill et al., 1998, 2011) or ρ_a (Bowers et al., 2017; Braithwaite et al., 2010; Hill et al., 2013; Mikkelsen & Pejrup, 2001) individually obeys a fractal relation, with F representing the flocs' characteristic fractal dimension in either case.

Assuming that the above fractal model holds, the knowledge of bulk ρ_a along with observations of $\Delta\rho$ as a function d_f can be used to determine F, ρ_p, and d_p. The various relations to be combined (which are expanded upon in Section 3.2.2) are as follows: With volume concentration (VC) known across all size class bins (i) of the PSD from a LISST-100X and/or particle camera, total suspended solids (TSS_F) in terms of mass concentration can then be predicted from summing ρ_a multiplied by VC for each size class bin (i):

$$TSS_F = \frac{M_p}{V_s} = \sum_{d_{\min}}^{d_{\max}} \left\{\frac{M_p}{V_p + V_w}\right\}_i \left\{\frac{V_p + V_w}{V_s}\right\}_i = \sum_{d_{\min}}^{d_{\max}} \left\{\rho_a\right\}_i \left\{VC\right\}_i \tag{6}$$

where ρ_a is given by Equation 5 (Babin et al., 2003; Braithwaite et al., 2010; Ganju et al., 2007). In Equation 6, V_s represents the total volume of the sample, and subscript F is used to denote TSS estimated from ρ_a and VC. TSS_F is matched to TSS determined from filtered water samples. In addition, observations of $\Delta\rho$

versus d_f from a video settling tube are fit to Equation 4. Finally, Equation 3 is used to relate $\Delta\rho$ to ρ_a as a function of ρ_p. An iterative solution to all of these equations simultaneously and uniquely solves for ρ_p and d_p using observations of PSDs, F, and TSS.

3. Method

3.1. In Situ Sampling and Instrumentation

Observations of particle properties were collected from surface waters of the York River estuary (Figure 1) using the Virginia Institute of Marine Science (VIMS) Coastal Hydrodynamics & Sediment Dynamics (CHSD) lab's water column profiler (Figure 2). The York is a partially mixed, microtidal estuary, and spans 50 km from West Point to Gloucester Point (Friedrichs, 2009). With VIMS located on the shore of the estuary, the York is a logistically attractive site to observe flocs having a wide range of characteristics. The York exhibits persistent spatial patterns in stratification, physical mixing, suspended sediment, and organic matter concentrations along its main axis (Friedrichs, 2009; Moore et al., 1997; Schaffner et al., 2001). The middle to upper York oscillates between partially and well-mixed conditions, and compared with the Lower York, tends to have more intense tidal currents, a greater range of salinities, and higher suspended sediment concentrations (Friedrichs, 2009). A primary estuarine turbidity maximum (ETM) occurs upstream near West Point, and the middle York seasonally experiences the intermittent presence of a secondary turbidity maximum (Friedrichs et al., 2008; Moore et al., 1997). In the lower York the estuary deepens, and as a result, the water column in the lower estuary is generally more stratified, turbulence is weaker, and the suspended sediment concentrations are lower (Schaffner et al., 2001).

Instruments and sampling gear mounted on the CHSD profiler on the various cruises included the following: a Sequoia Scientific Laser in situ Scattering and Transmissometry instrument Type C (LISST-100X), a high-definition particle imaging camera system (PICS), a YSI-6600 or YSI-EXO2 conductivity, temperature, depth (CTD), and water quality sonde, a SonTek and/or Nortek acoustic Doppler velocimeter (ADV) for current speed, and a high-speed pump sampler with an intake hose at approximately the same height as the LISST-100X (Figure 2). The LISST-100X was mounted on the profiling frame with its sampling window close enough to the PICS to assume that the two instruments were sampling near-surface floc populations

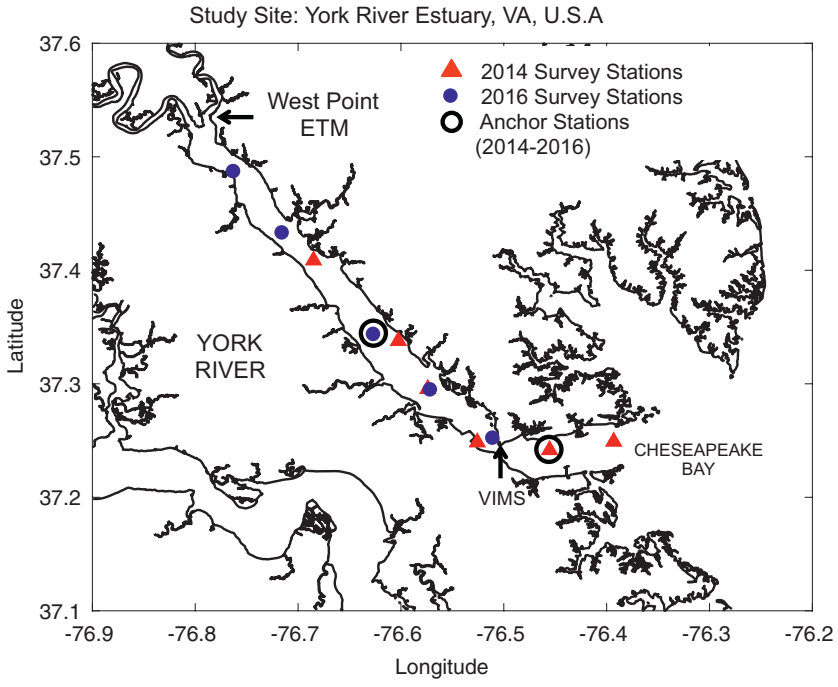

Figure 1. Map of the York River estuary. Profiler survey locations are indicated by the red triangles (2014) and blue circles (2016). Anchor station locations are circled in black (2014–2016).

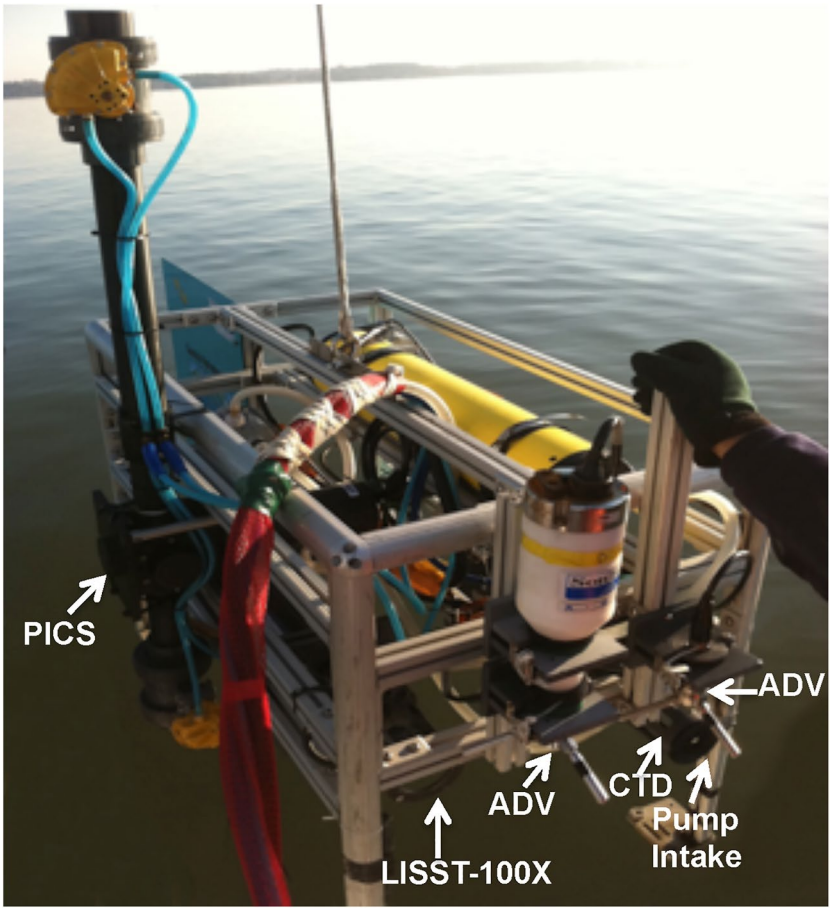

Figure 2. Photograph of the CHSD water column profiler indicating the position of the pump sampler's intake, along with the PICS, LISST-100X, CTD, and ADVs. Photograph by G. Massey. LISST, Laser in situ Scattering and Transmissometry.

with similar statistical properties. At each sampling station, the profiler was deployed off the 9-m VIMS R/V Ellis Olsson, lowered to a depth of 1–3 m below the surface, and kept there while the suite of instruments sampled for 2–5 min.

Water samples collected by the high-speed pump were analyzed for TSS and organic content via standard gravimetric analysis combined with loss on ignition (LOI; USEPA, 1983 Methods No. 160). Pumped samples were placed in 500-ml dark plastic bottles, stored in an ice chest on deck, and filtered immediately upon returning to VIMS (<8 h later). Vacuum filtering was employed utilizing preweighed, 0.7 μm, 47-mm diameter glass fiber filters. After filtration, the filters were rinsed with deionized water to remove salt and were then oven-dried at 103°C–105°C for at least 24 h. The filters were reweighed and redried repeatedly until consecutive weights agreed to within 0.5 mg. The filters were then placed in a 540°C oven for at least an hour, allowed to cool, and reweighed to determine the relative organic content via LOI.

Observations were collected on 10 cruises between September and December over the course of 3 years (2014–2016). Samples were collected in the fall and early winter to avoid phytoplankton blooms, which are most likely to occur during spring and summer in this system (Reay, 2009; Sin et al., 1999). An aim of this study was to examine the properties of flocculated particles near the water surface using observations that had not been significantly confounded by the presence of relatively large algal cells. Four of the cruises surveyed six stations along the York, spaced between the estuary mouth and roughly 20 km downstream of the main ETM. Each station was sampled once on the same day. For the other six cruises, the vessel was anchored at one station, and samples were collected once in an hour for half of a tidal cycle (~6 h), bracketing either a flood or ebb tide. One anchor station was completed in the lower York while the others were done in the middle York.

3.2. Determining Floc Size (d_f), Settling Velocity (w_s), and Excess Density ($\Delta\rho$) Using the PICS

The PICS video camera system (Figure 2) was developed to collect in situ measurements of particle diameter and settling velocity, which are then combined to estimate the particle excess density (Smith & Friedrichs, 2011, 2015). The PICS unit utilized here consists of a meter-long settling column with a 5-cm inner diameter, a 1.4-mega-pixel digital video camera, and a 1-mm thick, 635-nm wavelength laser light sheet. The thin laser sheet optimizes the sharpness of the camera's focus, but it limits the largest size of fully resolved flocs to ~1 mm. (Larger flocs, if present will be seen, but they will not be entirely contained within the thickness of the laser sheet.) At each end of the settling column are two pneumatically controlled ball valves used to open and close the settling column. The valves are kept open as the profiler is lowered to the desired sampling depth. The two ball valves are then closed, and water motion within the tube is allowed to dissipate for ~15–30 s. A 30-s video is then captured at 8 frames/s. The imaged region within the settling column is approximately 14 × 10 × 1 mm with a resolution of 1,360 × 1,024 pixels, i.e., 1 pixel ≈ 10 × 10 μm (Smith & Friedrichs, 2015).

The automated image processing routines developed by Smith and Friedrichs (2015) combine particle tracking velocimetry (PTV) with automated particle image velocimetry (PIV) to identify and track particles between successive image frames, estimate background fluid velocity, and measure the floc size (d_f) and settling velocity (w_s). These were applied here to identify and track particles in time across adjacent frames (PTV), while simultaneously assessing the motion of smaller particles (≤2 pixels in diameter) via spatial cross-correlation between frames to estimate the background fluid velocity (PIV). With PTV, for a frame-to-frame particle match to be accepted, a correlated particle must change in the estimated cross-sectional area by no more than 25%, and the ratio of its minor-to-major dimensions must change by no more than 15% over a least five frames (Smith & Friedrichs, 2015). In addition to improving the quality of the w_s estimates, these stringent matching criteria also help ensure that the size and shape of the accepted particles have been accurately determined. The frame-averaged PIV velocity is then subtracted from each PTV velocity to produce an averaged estimated of w_s for each tracked particle. In order to reliably track particles, image processing requires particles to appear in an area of at least 3 × 3 pixels or greater (Mikkelsen et al., 2004; Milligan & Hill, 1998; Sanford et al., 2005; Smith & Friedrichs, 2011). The PICS minimum resolvable size for PTV is thus 30 μm. For suspended mass concentrations of flocs of the order of 10 mg/L or more during a typical 30-s video, 1,000 or more distinct particles ≥ 30 μm in size are typically assigned individual w_s values.

Finally, concurrent measurements of w_s and d_f are used to estimate the excess density ($\Delta\rho$) for each tracked particle by rearranging Soulsby's (1997) empirically derived Stokes-like, expression for settling velocity:

$$\Delta\rho = \rho_f - \rho_w = \frac{\rho_w \upsilon^2}{g K_2 d_f^3}\left[\left(\frac{w_s d_f}{\upsilon} + K_1\right)^2 - K_1^2\right] \tag{7}$$

where g is the gravitational acceleration, υ is the kinematic viscosity, and K_1 and K_2 are the empirical constants ($K_1 = 10.36$, $K_2 = 1.049$). The water properties (ρ_w, υ, and temperature) used in Equation 7 were determined from measurements of the conductivity, temperature, and pressure collected with the profiler's CTD.

3.3. Determining PSDs With the LISST-100X

A Sequoia Scientific LISST-100X Type C instrument was deployed to provide an additional independent measurement of particle size and to better account for smaller flocs in suspension. Although the LISST-100X cannot track and measure individual particles, it can be used to resolve reliable PSDs in situ for a range of particle sizes, shapes, and compositions (e.g., Agrawal et al., 2008; Agrawal & Pottsmith, 2000; Andrews et al., 2010; Bowers et al., 2011; G. M. Cartwright et al., 2011; Fettweis & Baeye, 2015; Fugate & Friedrichs, 2003; Hill et al., 2011). The LISST-100X emits a collimated beam of light (at 670 nm) through an in situ sample and measures the intensity of that light that is scattered onto 32 concentric ring detectors. The pattern of scattered light is numerically inverted using an instrument-specific calibration matrix to estimate the particle volume concentrations for 32 logarithmically spaced size classes (Agrawal & Pottsmith, 2000). The LISST-100X Type C, which was used in this study, measures the size distribution of volume concentration from 2.5 to 500 μm. At each station, the LISST-100X sampled for bursts of 2–5 min, coincident

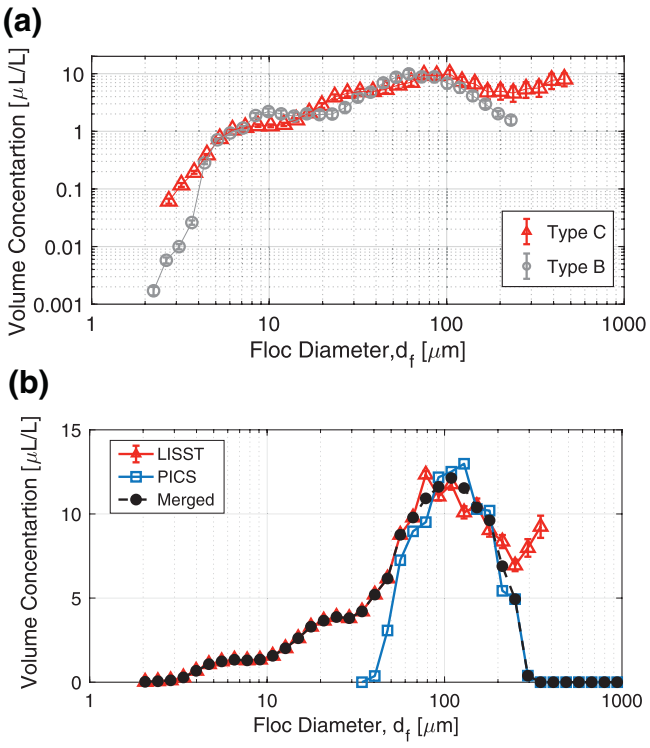

Figure 3. (a) A comparison of the average particle volume concentration distributions (PSD) for 12 co-located samples collected by Type C and Type B LISST-100X instruments in September 2016. (b) An example sample illustrating the merging of LISST-100X Type C and PICS particle volume size distributions. LISST, Laser in situ Scattering and Transmissometry.

in time with the collection of PICS data and water samples. LISST-100X PSDs were collected at 1 Hz, and the mean PSD over the duration of each burst was used in subsequent analysis. Sequoia Scientific's random shape scattering property kernel matrix was used to invert the data collected in this study.

When using the LISST-100X series of instruments, it is important to be aware of its tendency to produce "rising tails" in the estimated volume concentration at the lowermost and uppermost ends of its PSD range. Rising tails can lead to misrepresentation of the actual size distribution. Rising tails at larger particle sizes are relatively common in the LISST-100X output and can be due to the presence of large particles that are outside of the instrument's resolvable size range, increased sensitivity of larger particles to refractive index effects, and/or the greater uncertainties inherent in resolving very small scattering angles (Agrawal & Pottsmith, 2000). Observations from the PICS can be used in place of rising tails at the upper end of the LISST's range (see description of PSD merging in Section 3.4). At the lower end of its range, the presence of particles smaller than 2.5 μm may increase the volume of particles estimated in the smallest size classes by the LISST-100X Type C (Andrews et al., 2010). Excess ambient light, which impinges on the outer rings, can also increase the apparent particle volume assigned to the smallest size classes (Andrews et al., 2010; Reynolds et al., 2010), as can the presence of irregularly shaped particles, which scatter at wider angles than spheres (Agrawal et al., 2008). However, the relatively turbid water of the York River estuary implied that ambient light contamination was probably not a significant issue (optical transmission <0.9 for all samples), and inversion with Sequoia's random shape matrix was performed in an effort to alleviate concerns associated with irregularly shaped particles.

In September 2019, a LISST-100X Type B was deployed approximately 2 m below the surface at the CHSD long-term observing station, which provided an opportunity to further consider the possible effects of smaller, out-of-range particles on the LISST-100X Type C response. The smallest bin of the Type B is centered at 1.25 μm, compared to 2.5 μm for the Type C. Twelve sampling stations during this study were visited, where both the LISST Type C and LISST Type B were used to obtain samples for overlapping time periods. Overall, the average PSDs from the two instruments agreed quite well for diameters between ~4 and 175 μm (Figure 3a). Type B showed a strong decrease in volume concentrations for size bins between 1.25 and 4 μm. In fact, the concentration for bins below 2 μm was found to be below the detection limit of Type B. In contrast, the average Type C PSD showed a less intense decrease over its two smallest size bins. Recognizing that the vertical axis in Figure 3a is logarithmic, this difference represents a negligible portion of the overall particle volume distribution observed by either instrument. Both the results suggest that the Type C is not under-sampling or otherwise missing a significant concentration of very small particles.

3.4. Merging LISST-100X and PICS PSDs

The output from the PICS was used to provide a relative measure of the particle volume distribution as a function of floc size, but not as an absolute measure of the total volume concentration. The total volume of particles measured by the PICS is dependent on the background speed of the water in its settling column and also on the overall fraction of particles which pass its criteria for reliable size and shape at a given station (Smith & Friedrichs, 2011, 2015). Therefore, for each PICS sample, the absolute volume measured by the PICS was scaled by matching the PICS and LISST-100X volume concentrations across their overlapping bins. Despite analogous challenges, others have successfully merged LISST-100X and camera-based observations of floc size and volume concentration in similar coastal and estuarine environments in order to expand the observed particle size range and overall quality of PSDs toward higher floc sizes (Hill et al., 2011; Mikkelsen et al., 2005, 2006).

In this study, PICS and LISST-100X PSDs were merged following a scaling methodology similar to that introduced by Mikkelsen et al. (2005). Particle volumes measured by the PICS as a function of particle size (V_{PICSi}) were binned into 23 logarithmically spaced size bins from 30 to 1,000 μm, chosen to match and extend the bin sizes used by the LISST-100X. As in Mikkelsen et al. (2005), the LISST-100X was chosen as the reference instrument, and V_{PICSi} (in mm^3 per bin) was multiplied by a scaling factor (α) to estimate the equivalent PICS volume concentration in each bin, VC_{PICSi} in μL/L (same units as the LISST-100X). The parameter α was determined for each sample by calculating the average ratio of LISST-100X volume concentration to PICS volume over a set range of n overlap bins $i{:}i+n$:

$$\alpha = \frac{\overline{VC_{\mathrm{LISST_{i:i+n}}}}}{V_{\mathrm{PICS_{i:i+n}}}} \tag{8}$$

The range of the overlap bins ($i{:}i+n$) was determined individually for each following Mikkelsen et al. (2005), based on the cumulative volume statistics, d_{25v}, d_{50v}, and d_{75v}. The overlap range with the strongest agreement between the two instruments was used to calculate α. The volume in all 23 of the PICS bins was multiplied by α to calculate the volume concentration (VC_{PICS}) in units of μL/L. Finally, the PICS and LISST-100X distributions were merged (Figure 3b). For bin size classes with lower limits of $i = 2$ μm to the lower value of overlap region, VC_i was assumed equal to VC_{LISSTi}; and for i = upper value of overlap region to 1,000 μm, VC_i was assumed equal to VC_{PICSi}. Within the overlap region, VC_i was set equal to the average of VC_{LISSTi} and VC_{PICSi}.

3.5. Determination of Fractal Floc Properties From Observations of Δρ, PSDs, and TSS

The primary particle density (ρ_p) and size (d_p) were determined by combining video-derived fractal properties, merged PSDs, and pump sampling. The steps in this calculation, as illustrated in Figure 4, were as follows: (1) values of w_s observed by the PICS were converted to Δρ using Equation 7. Then, through rearranging Equation 4:

$$\log(\Delta\rho) = \log\left[\left(\rho_p - \rho_w\right)d_p^{3-F}\right] - \left(3 - F\right)\log\left(d_f\right) \tag{9}$$

fractal dimension, F, was determined from the slope of the log-log best-fit of Δρ versus d_f as observed by the PICS. (2) Next, a range of possible ρ_p from 1,000:3,000 kg/m^3 was considered. For each of these possible ρ_p values, Equation 3 was used to determine ρ_a as a function of d_f over the range of bins contained in the PSD. Note that in log–log space, ρ_a always appears offset and parallel to Δρ (Figure 4). This is because, if one assumes a fractal model, the ratio of ρ_a to Δρ always equals $(1 - \rho_w/\rho_p)^{-1}$. For each of these possible ρ_p values, a unique corresponding d_p was determined from the constant term in the best-fit to Equation 9 (i.e., log $[(\rho_p - \rho_w)\, d_p{}^{3-F}]$), given that F was already known from the best-fit slope. For any particle diameters present in the PSD for sizes below d_p, it was assumed that $\rho_a = \rho_p$ (following Bowers et al., 2017 and Braithwaite et al., 2010). (3) The resulting values of ρ_{ai} were matched to each PSD bin, multiplied by the observed PSD volume concentration (VC_i) in each size class, and summed to predict a range of fractal estimates of TSS_F. (4) Finally, the case for TSS_F which most closely matched TSS determined from pump sampling was chosen as the best-case fractal model with the best corresponding values of ρ_p and d_p.

Pump samples were used to calculate an additional estimate of ρ_p, denoted as ρ_{tss}, using the fraction of organic material (f_{org}) determined via LOI along with estimates of the respective densities of the two fractions (ρ_{org} and ρ_{inorg}):

$$\rho_{\mathrm{tss}} = \frac{M_T}{V_T} = \frac{M_{\mathrm{inorg}} + M_{\mathrm{org}}}{V_{\mathrm{norg}} + V_{\mathrm{org}}} = \left[\frac{1 - f_{\mathrm{org}}}{\rho_{\mathrm{inorg}}} + \frac{f_{\mathrm{org}}}{\rho_{\mathrm{org}}}\right]^{-1} \tag{10}$$

(similar to Markussen & Andersen, 2013). For simplicity, the density of organic and inorganic solids, ρ_{org} and ρ_{inorg}, were assumed to be constants in this study, where $\rho_{inorg} = 2{,}750$ kg/m^3 and $\rho_{org} = 1{,}000$ kg/m^3 were chosen based on the values suggested in the literature for inorganic estuarine clays (Mehta, 2014) and for organic matter from estuarine plankton detritus (Wakeham & Canuel, 2016).

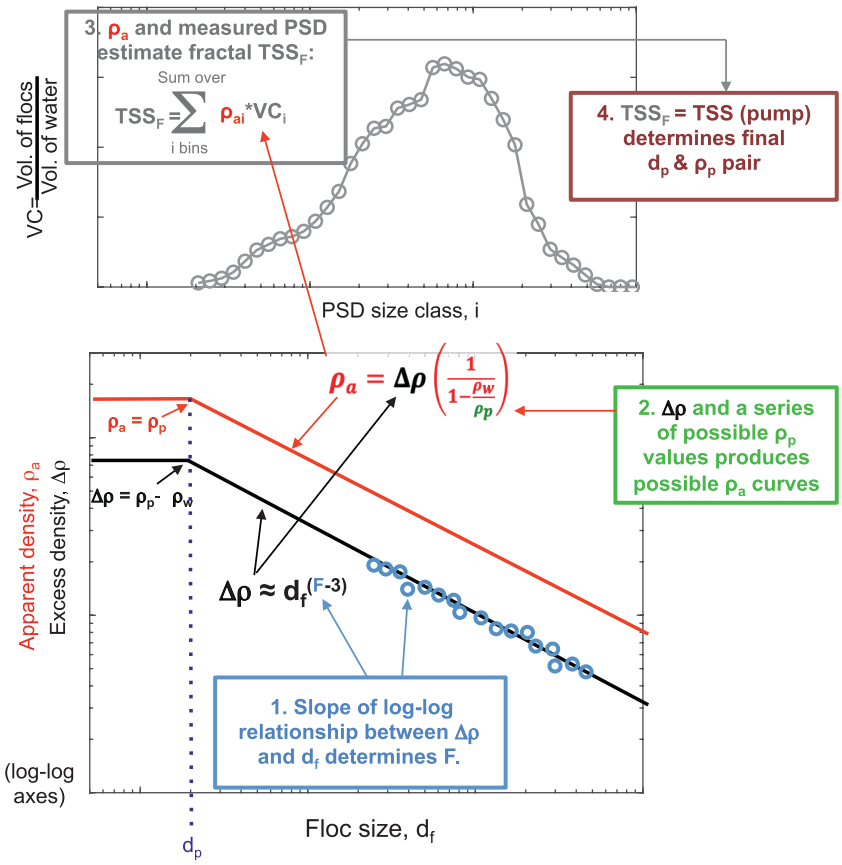

Figure 4. Conceptual model that depicts how the theoretical relationship between $\Delta\rho$ and ρ_a is combined with fractal approximations inferred from video settling analysis (*PICS*) and observed particle size distributions (*LISST/PICS*) to determine primary particle size (d_p) and density (ρ_p). LISST, Laser in situ Scattering and Transmissometry.

4. Results

4.1. Bulk Floc Characteristics and Their Relationships With Each Other and with Environmental Conditions

The suspended floc characteristics were measured for 65 independent samples, collected over a variety of hydrodynamic conditions and for a range of sediment concentrations, organic fractions, and bulk apparent densities. Coinciding with the sample collections, current speed (U) varied from 2 to 60 cm/s, and salinity (S) ranged from 16 to 22 ppt. Although TSS mass concentrations ranged from 8 to 88 mg/L, more than 50% of the TSS samples were less than 25 mg/L. The bulk organic fraction (f_{org}) of TSS ranged from 0.13 to 0.46, resulting in primary particle density (ρ_{tss}) calculated from Equation 10 ranging from 1,620 kg/m^3 to 2,230 kg/m^3. Recall that the organic fraction was determined using LOI (Section 3.1), so the values represent relative measures of organic content defined as material volatized or burned off at 550°C. Sampling cruises targeted the times of low productivity in the system, so it is assumed that the bulk of this is attributed to nonliving organic detritus rather intact plankton cells. The values for ρ_{tss} are lower than that of pure clay minerals and higher than purely organic material, but are consistent with the hypothesis that primary particles are not simply clusters of clay minerals, but rather exist as small aggregates composed of both inorganic minerals and less dense organic material (Braithwaite et al., 2010; Fettweis, 2008; Maggi, 2013; Markussen & Andersen, 2013). The bulk apparent density (ρ_{a_bulk}), calculated by dividing TSS by the total floc volume (from PSDs), ranged from 210 to 1,920 kg/m^3.

Merged LISST-100X/PICS PSDs revealed that the majority of the volume in suspension was contained within microflocs or smaller flocculi, with approximately 80% attributed to particles less than 100 μm in diameter (Figure 5). Flocculi are defined here as the smallest aggregates composed of primary particles

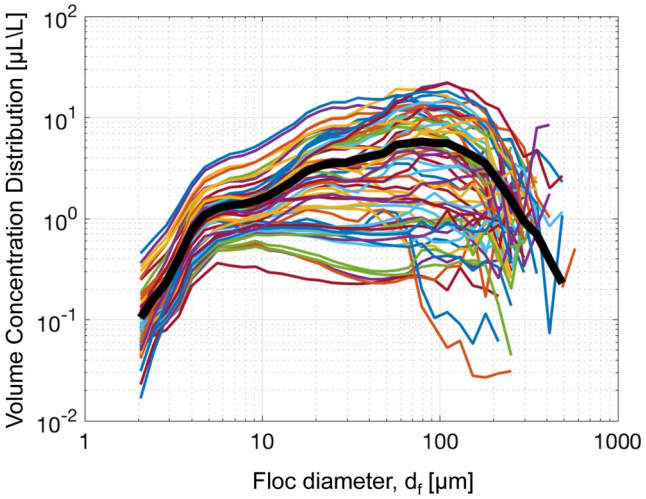

Figure 5. *LISST + PICS* merged particle size distributions. The solid black line represents the overall average particle size distribution. LISST, Laser in situ Scattering and Transmissometry.

and water. Flocculi are seldom broken apart and are thus considered as a major building block of somewhat more fragile microflocs (Lee et al., 2012). Transitions from flocculi to microflocs and from microflocs to macroflocs are commonly defined within the neighborhoods of 35–50 and 130–200 µm, respectively (Lee et al., 2012; Mikkelsen et al., 2006). When presented in log-log format, the PSDs in this study appeared fairly widely distributed over ~4–300 µm. However, the median particle size by volume (d_{50v}) was always found to be within the range of flocculi to microflocs, spanning 15–90 µm, with an average of 45 ± 2 µm. (Unless stated otherwise, ± throughout this paper indicates one standard error.) The average PSD of all samples is plotted as a solid black line in Figure 5. It was characterized by a moderately multimodal signal, with slight peaks between 4–8 and 20–30 µm, and a more prominent peak around 70–100 µm.

Correlations among variables showed that a lower S and a greater U led to a higher TSS, and a higher TSS, in turn, favored a larger d_{50v}, lower f_{org}, and lower ρ_{a_bulk}. TSS was significantly correlated to S (Figure 6a), consistent with TSS increasing along-channel toward the ETM as S decreased. (For statistical comparisons, significance here is defined as p-value < 0.05). TSS had a notably stronger, positive dependence on U (Figure 6b), consistent with the sediment resuspension. In fact, TSS was correlated more strongly with U than with any other variable examined. U was less strongly but still significantly correlated with d_{50v} (positively), f_{org} (negatively), and ρ_{a_bulk} (negatively). However, the magnitudes of these correlations with U were each smaller than their corresponding correlations with TSS. This supports the interpretation that as U increased, greater concentrations of flocs were suspended into the surface waters. Greater floc concentrations (i.e., higher TSS) were, in turn, associated with larger diameter, less organic, and less dense flocs (i.e., containing more interstitial water; Figures 6c–6e). The possible effects of increased U enhancing turbulence, breaking flocs apart, and reducing d_{50v} were likely overwhelmed by the effect of increased U suspending higher concentrations of larger flocs into the surface waters.

The variables d_{50v} and ρ_{a_bulk} were also significantly correlated to f_{org}, and, consistent with the fractal behavior, ρ_{a_bulk} and d_{50v} were strongly related via a decreasing power law. As f_{org} increased, it was observed that d_{50v} decreased and ρ_{a_bulk} increased (Figures 6f and 6g), with relationships even stronger than their responses to TSS. In one respect, an increase in ρ_{a_bulk} with greater organic fraction may seem counterintuitive, because, all else being equal, organics are less dense than clay minerals. Thus, mitigating factors that overcame the underlying density difference between organic matter and clay were likely present, such as systematic variations in fractal properties and/or characteristic floc size as a function of organic content. The relatively strong correlation and negative power-law relationship between ρ_{a_bulk} and d_{50v} (Figure 7) suggest fractal floc behavior with a bulk fractal dimension, F_{bulk}, of 2.25 ± 0.09. We use the term "bulk" here, because the power law was fit between ρ_{a_bulk} and d_{50v}, parameters for size and density that each describe populations (or bulk samples) of particles, rather than observations of size (d_f) and density ($\Delta\rho$) from individual particles. The blue dashed lines in Figure 7 highlight data falling 40% above or below values for ρ_{a_bulk} predicted by the solid back best-fit line. It is worth noting that the residuals above or below the blue dashed lines are significantly related to f_{org}, such that a higher f_{org} favors positive residuals, while a lower f_{org} favors negative residuals. This suggests that, relative to the overall best-fit relationship between ρ_{a_bulk} and d_{50v}, higher and lower ρ_{a_bulk} is associated with higher and lower organic content, respectively.

4.2. Fractal Floc Properties Determined From Pooling PICS Observations

Before pooling or otherwise bin-averaging PICS observations, there was a high degree of scatter seen between settling velocities (w_s), excess densities ($\Delta\rho$), and floc diameters (d_f) for individual particles (Figures 8a and 8b). This is not unique or unexpected. Unlike individual mineral grains, w_s and $\Delta\rho$ for flocs are not only correlated to the grain's size and mineral density, rather, they are also influenced by the variable organic and

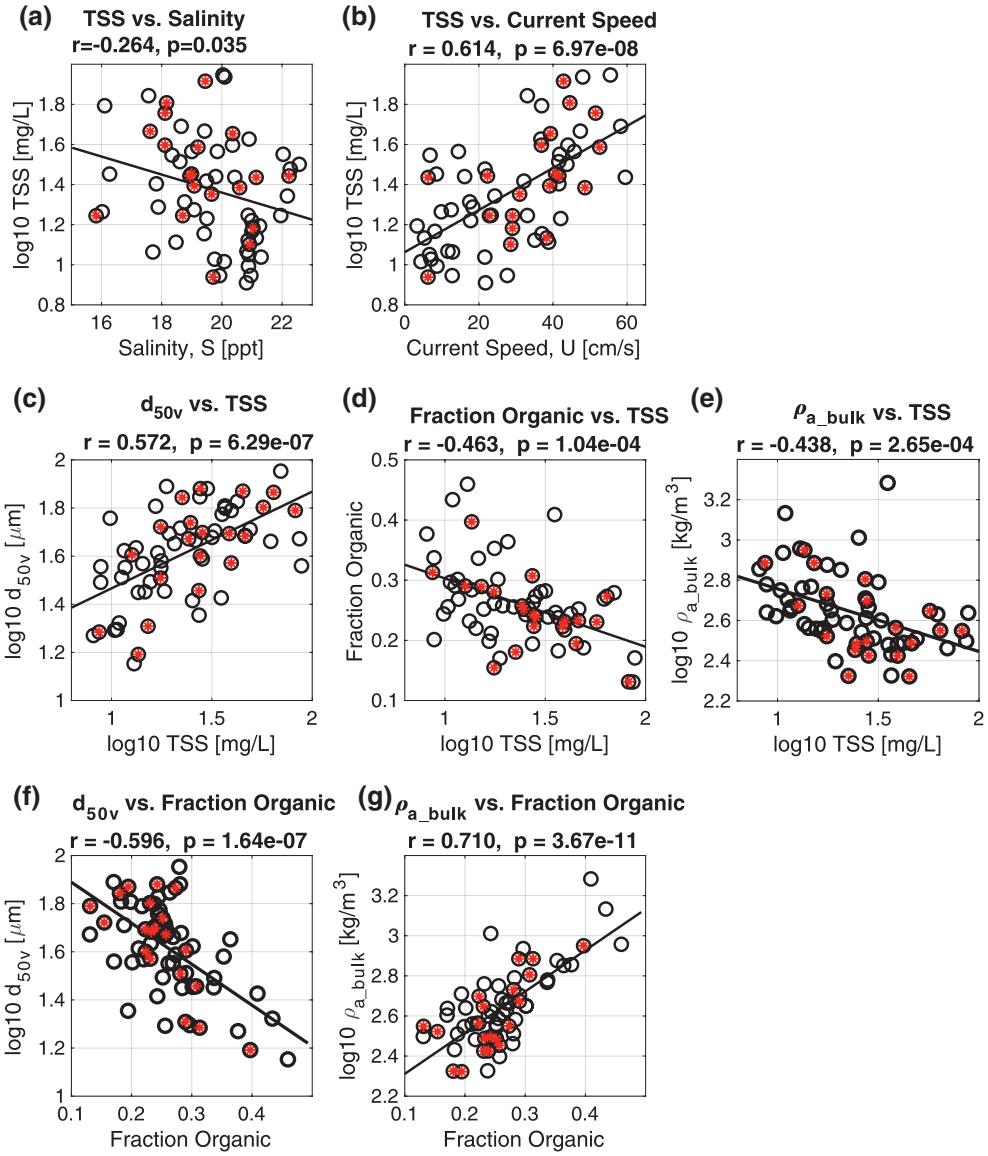

Figure 6. Regressions among variables describing bulk floc conditions including (a) total suspended solids (tss) vs. salinity, (b) tss vs. current speed (U), (c) median particle size as a function of volume (d_{50v}) vs. tss, (d) fraction organic matter vs. tss, (e) bulk apparent density (ρ_{a_bulk}) vs. tss, (f) d50v vs. fraction organic, and (g) ρa_bulk vs. fraction organic matter. Black circles are all 65 samples. Circles containing red stars indicate the 20 samples that could confidently be fit to the fractal model (see Section 4.3). Correlations (r) and p-values (p), and best-fit lines are for fits to all 65 samples. Variables are plotted as $\log_{10}$ values if their underlying histograms are log-distributed rather than normally distributed.

water content of their constituent particles (Winterwerp & van Kesteren, 2004). The amount of scatter seen here is similar to that observed in other environments with other video systems (Dyer & Manning, 1999; Fettweis, 2008; Hill et al., 1998; Khelifa & Hill, 2006; Maggi, 2013). In addition to the more complicated nature of settling of cohesive flocs, much of the noise here was associated with the PICS instrumentation. Despite using automated PIV analysis for improved estimates of background fluid velocity (Smith & Friedrichs, 2015), not all water motion appeared to be accounted for in postprocessing, resulting in negative values in both w_s and $\Delta\rho$ for some samples. Accurate PIV analysis requires large numbers of observations of PIV-sized particles (Smith Friedrichs, 2015). This presents challenges in surface waters with low suspended sediment concentrations and with less than ideal camera lighting (see "Discussion"). The scatter among the individual observations (>100,000 floc in total) was greatly reduced by averaging the w_s and $\Delta\rho$ measurement over 75 logarithmically spaced particle size bins extending from 30 to 1,000 μm (Figures 8c and 8d).

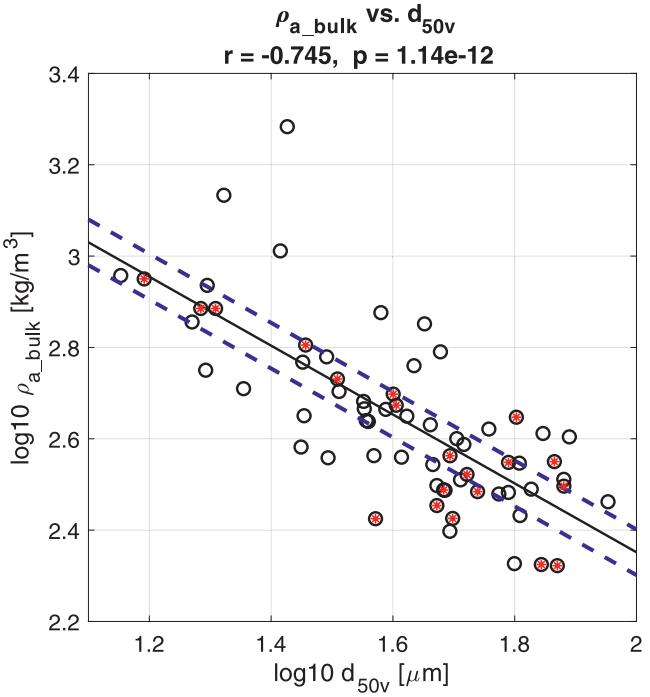

Figure 7. Bulk apparent floc density (ρ_{a_bulk}) versus median floc diameter (d_{50v}). A bulk fractal dimension, $F_{bulk} = 2.25 \pm 0.09$, was determined by a best-fit of log (ρ_{a_bulk}) to log (d_{50v}; solid black line). Dashed blue lines highlight data falling 40% above or below values predicted by the solid black best-fit line. Circles with and without red stars are as described in the caption of Figure 6.

Bin-averaging all samples of w_s and $\Delta\rho$ suggested the presence of two distinct fractal behaviors, applying separately to microflocs and macroflocs, with a change in slope or breakpoint occurring at ~150 μm. In order to avoid the influence of the curvature in slope near the breakpoint on the best-fit fractal dimensions, the fractal relations were approximated separately as best-fits for 40–100 μm (F_{micro}) and for >175 μm (F_{macro}). The resulting values for F_{micro} and F_{macro} inferred from bin-averaged w_s were 2.55 and 2.08 and from bin-averaged $\Delta\rho$ were 2.54 and 2.05 (Figures 8c and 8d). To ensure that the inferred fractal trends were not a result of bin-averaging over 75 bins specifically, $\Delta\rho$ and w_s were also averaged over 50 and 100 size class bins. The fractal approximations were insensitive to the number of size class bins. Applying the different means of averaging (50, 75, or 100 bins), estimates of F_{micro} and F_{macro} varied from 2.52–2.56 to 2.04–2.14, respectively. The larger variability in F_{macro} was expected due to fewer observations of larger particles. The $\Delta\rho$ was derived from the observed w_s (Equation 7), so it is not surprising that the fractal dimensions determined from each variable was similar. This study utilizes the theory based on $\Delta\rho$, so for the remainder of the analysis, fractal relationships were determined solely from the relationship between $\Delta\rho$ and d_f. Despite the visually striking breakpoint between F_{micro} and F_{macro}, it is important to note how little material is actually contained within the macroflocs in this environment. Taking $F_{micro} \approx 2.5$ and $F_{macro} \approx 2.1$ with a break at $d_f = 150$ μm, the average PSD in Figure 5 has only 4% of its dry mass contained in the macroflocs.

A main goal of this study was to investigate the possible role of organic matter in affecting the fractal properties of flocs, so observations of flocs were also pooled into high and low organic content end-members (Figure 9). The observations in this study captured the well-documented gradient in TSS and organic matter content found along the York River

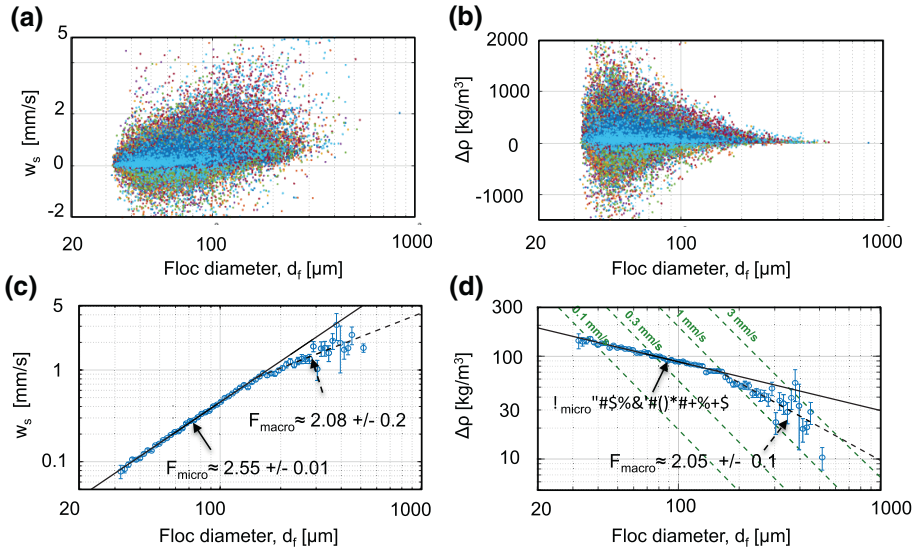

Figure 8. *PICS* measured floc size (d_f) versus (a) floc settling velocity (w_s) and (b) calculated floc excess density ($\Delta\rho$) for all particles tracked. Colors differentiate the 65 independent samples to help visualize individual observations. Bin-averaged (c) w_s and (d) $\Delta\rho$ over 75 logarithmically spaced particle size bins from 30 to 1,000 μm. Best-fit fractal models indicated with black lines. Error bars and ± indicate standard errors. Dashed green lines on D show the $\Delta\rho$ over entire size range assuming a constant settling velocity, specifically for w_s = 0.1, 0.3, 1, and 3 mm/s (from left to right, respectively).

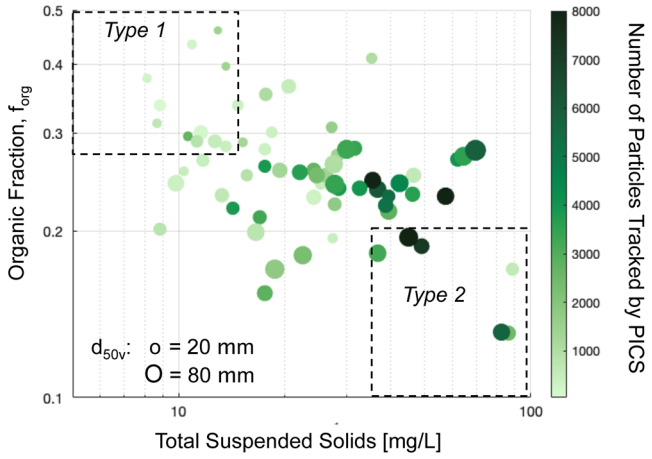

Figure 9. The relationship between Type 1 and Type 2 samples and the general properties of suspended particles sampled in surface waters of the York River estuary. Symbol color indicates the number of particles tracked by the *PICS* in each sample, and symbol size corresponds to median particle size by volume (d_{50v}) determined for the PSD for that sample. Type 1 samples were simultaneously the highest 20% for f_{org} and lowest 20% for *TSS*, while Type 2 samples were the opposite.

estuary (Friedrichs, 2009; Moore et al., 1997; Schaffner et al., 2001). The highest organic content samples collected farthest downstream from the ETM also had among the lowest TSS values. This meant that for individual samples with a high f_{org}, there were often too few particles successfully tracked by the PICS to produce a reliable and/or statistically stable fit to a fractal model. In order to have enough particles to be able to use the PICS to examine the difference in fractal characteristics at high versus low organic content, end-member samples were pooled into corresponding Type 1 and Type 2 suspensions (Figure 9). Type 1 suspensions were defined as samples that were in the upper 20% in terms of organic fraction ($f_{org} > 0.28$) and lower 20% in terms of TSS (TSS < 15 mg/L). This group was made up of 12 samples in total. Type 2 suspensions were defined as samples that were in the upper 20% of TSS (TSS > 37 mg/L) and lower 20% of organic fraction ($f_{org} < 0.2$), and consisted of six samples (albeit with each sample containing many more particles).

PSDs were found to be distinctly different for Type 1 versus Type 2 suspensions with regard to both PSD shape and d_{50v} (Figures 10a and 10b). PSDs for low organic content, high TSS (Type 2) suspensions were fairly narrow and unimodal, with a peak around 50–100 μm (Figure 10a), while organic-rich, low TSS (Type 1) suspensions were characterized by a wider and flatter PSD, with a slight peak around 5–20 μm (Figure 10b). Average d_{50v} was significantly higher for the Type 2 suspensions, $d_{50v} = 57 \pm 5$ μm compared to $d_{50v} = 25 \pm 2$ μm for Type 1. In terms of the multimodal classification of Lee et al. (2012), the lower concentration, organic-rich Type 1 suspensions contained a larger fraction of the total particle volume within primary particles/flocculi ($d_f < \sim 30$ μm). In contrast, the lower concentration, organic-poor Type 2 suspensions contained a larger fraction of particle volume within microflocs ($d_f \approx 40$–150 μm).

Pooled PICS data revealed that Type 1 (higher f_{org}, lower TSS) flocs had similar F_{micro}, and lower F_{macro} relative to Type 2 flocs (Figures 10c and 10d). Similar to the case containing all 100,000+ observed particles (Figure 8), the best-fit fractal relations for these two end-members also showed a change in slope around 150 μm, again separating microflocs and macroflocs. F_{micro} was slightly higher, but not significantly so, for Type 1 (2.62 ± 0.04) versus Type 2 (2.55 ± 0.02). In contrast, there was a significant difference between F_{macro} for Type 1 (high f_{org}) and Type 2 (low f_{org}) flocs, namely, $F_{macro} = 1.22 \pm 0.2$ and 2.23 ± 0.2, respectively. Despite the visually striking "kinks" or breakpoints in F, the calculations of ρ_p and d_p were insensitive to the properties of the macroflocs. This is because the vast majority of the total suspended mass was contained within flocs that are smaller than ~ 150 μm. To confirm this insensitivity, PICS fractal models and PSDs were first used to estimate ρ_p and d_p for Type 2 and Type 1 flocs using a single fractal fit (as illustrated in Figure 4), based on fitting the microflocs from 40 to 100 μm (solid black lines in Figure 10). Next, two fractal fits were considered, following a nearly identical procedure, but with the distinct second F_{macro} fit to macroflocs > 175 μm (dashed black lines in Figure 10). The results indicate that there was no significant difference in the best-fit values for ρ_p and d_p, whether the fitting approach used just F_{micro} or used both F_{micro} and F_{macro} (Figures 10c and 10d). This is important because later in the results, ρ_p and d_p values are calculated from individual samples containing data that were too noisy to resolve a distinct value for F_{macro}.

Additional measures of particle density, namely, macrofloc $\Delta\rho$, microfloc ρ_a, and bulk ρ_{tss}, were also different for the two end-members. Representative excess densities for 200 μm macroflocs ($\Delta\rho_{\_200\mu m}$) and 60 μm microflocs ($\Delta\rho_{\_60\mu m}$) for Type 1 and Type 2 cases were estimated by calculating the average densities of observed particles having d_f between 180–220 μm and 50–70 μm, respectively. This showed $\Delta\rho$ for high f_{org} macroflocs ($\Delta\rho_{\_200\mu m} = 51 \pm 6$ kg/m^3) to be only about 63% of that found for low f_{org} macroflocs ($\Delta\rho_{\_200\mu m} = 80 \pm 4$ kg/m^3). For the apparent density of microflocs, the trend was the opposite. Using the theoretical solutions for $\Delta\rho/\rho_a$ (Equation 3) and pooled particle groups from the $\Delta\rho_{\_200\mu m}$ and $\Delta\rho_{\_60\mu m}$ calculations, the representative apparent density of 200 μm macroflocs and 60 μm microflocs were determined. It was seen that ρ_a for high f_{org} microflocs ($\rho_{a\_60\mu m} = 421 \pm 14$ kg/m^3) was 1.5 times greater than that for low f_{org} microflocs

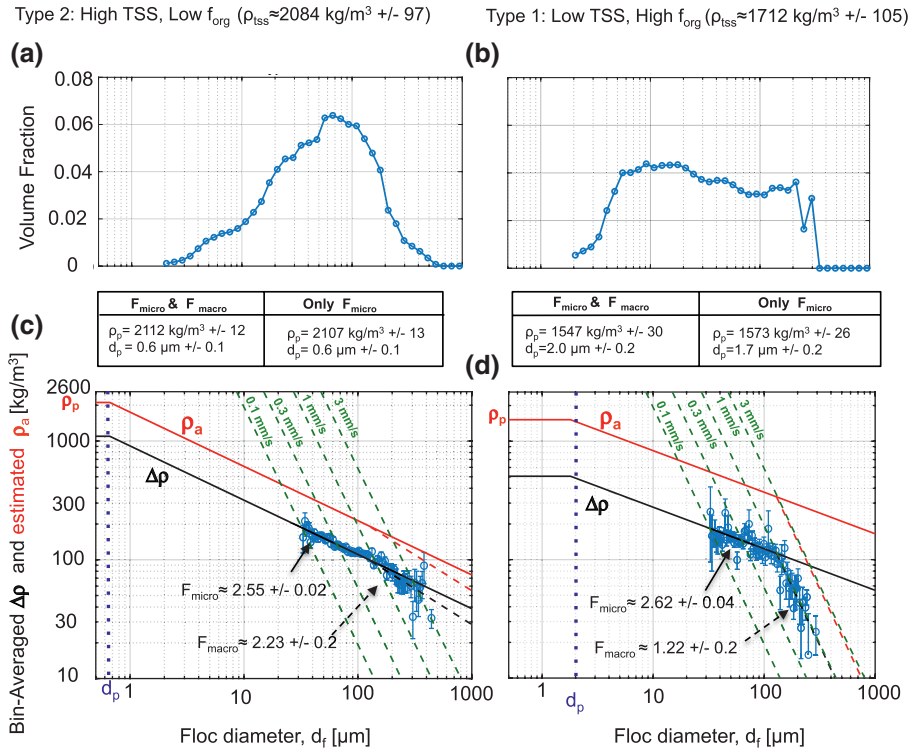

Figure 10. Comparison between flocs and fractal properties between Type 2 (low $f_{org,}$ high TSS) and Type 1 (high $f_{org,}$ low *TSS*) suspensions. Average particle size distributions for (a) Type 2 and (b) Type 1 suspensions. Bin-averaged $\Delta\rho$ versus d_f from samples pooled representing (c) Type 2 and (d) Type 1 suspensions. Plots of bin-averaged $\Delta\rho$ versus d_f used 75 bins, and best-fits to $\Delta\rho$ were calculated for 40–100 µm (black solid line, F_{micro}) and for >175 µm (black dashed line, F_{macro}). The red lines show corresponding theoretical values for ρ_a. The theoretical relationship between $\Delta\rho$ and ρ_a was used to estimate ρ_p and d_p as outlined in Figure 4. The inset displays result from assuming either two fractal components (F_{micro} and F_{macro}) or one fractal component (only F_{micro}). Dashed green lines on c and d show $\Delta\rho$ as a function of d_f for constant settling velocities, specifically for w_s = 0.1, 0.3, 1, and 3 mm/s (from left to right, respectively).

($\rho_{a\_60\mu m}$ = 277 ± 4 kg/m^3). The values for ρ_{tss} in Figure 10 are averages that follow directly from f_{org} via Equation 10, so it was not surprising that pooled ρ_{tss} for the organic-rich (Type 1) flocs (ρ_{tss} = 1,712 ± 107 kg/m^3) was significantly less than that for low f_{org} (Type 2) end-member (ρ_{tss} = 2,084 ± 97 kg/m^3). Despite their differences in $\rho_{a\_60\ \mu m}$ and $\rho_{tss,}$ the two end-members had effective densities for 60 µm flocs that were very similar (Type 1 $\Delta\rho_{\_60\mu m}$ = 145 ± 5 kg/m^3; Type 2 $\Delta\rho_{\_60\mu m}$ = 143 ± 2 kg/m^3). Thus the settling velocities for Type 1 and Type 2 60 µm flocs were also similar (as can be seen in Figures 10c and 10d). Variable organic matter content may not strongly affect $\Delta\rho$ or w_s for microflocs because the water and the organic matter the water displaces within the flocs both have wet densities of ~1,000 kg/m^3.

The best-fit values for ρ_p and d_p for the two end-members were significantly different, and the values for ρ_p were comparable to ρ_{tss}. Uncertainties for ρ_p and d_p displayed in Figure 10 are best-fit standard errors for the Type 1 and Type 2 end-members. Standard errors for ρ_{tss} for Type 1 and Type 2 particles in Figure 10 were inferred from the range of f_{org} observed for the pump samples within these groups. For organic-rich (Type 1) flocs, best-fit d_p = 2.0 ± 0.2 µm and ρ_p = 1,547 ± 30 kg/m^3. In contrast, more inorganic (Type 2) flocs had significantly lower d_p ≈ 0.6 ± 0.1 µm and significantly higher ρ_p ≈ 2,112 ± 12. Kg/m^3. For each of these two end-members, best-fit ρ_p was consistent with ρ_{tss} from pump samples (within ±2 standard errors). Also, best-fit d_p were within the range of previously established values (Braithwaite et al., 2010; Chapalain et al., 2018; Fettweis, 2008; Khelifa & Hill, 2006), and the observed increase in d_p with increased organic content is consistent with earlier findings of Maggi (2013). This suggests, at least in a bulk sense, that simple fractal approximations can describe surface flocs in the York River estuary, and that as these flocs become more organic, ρ_p decreases and d_p increases.

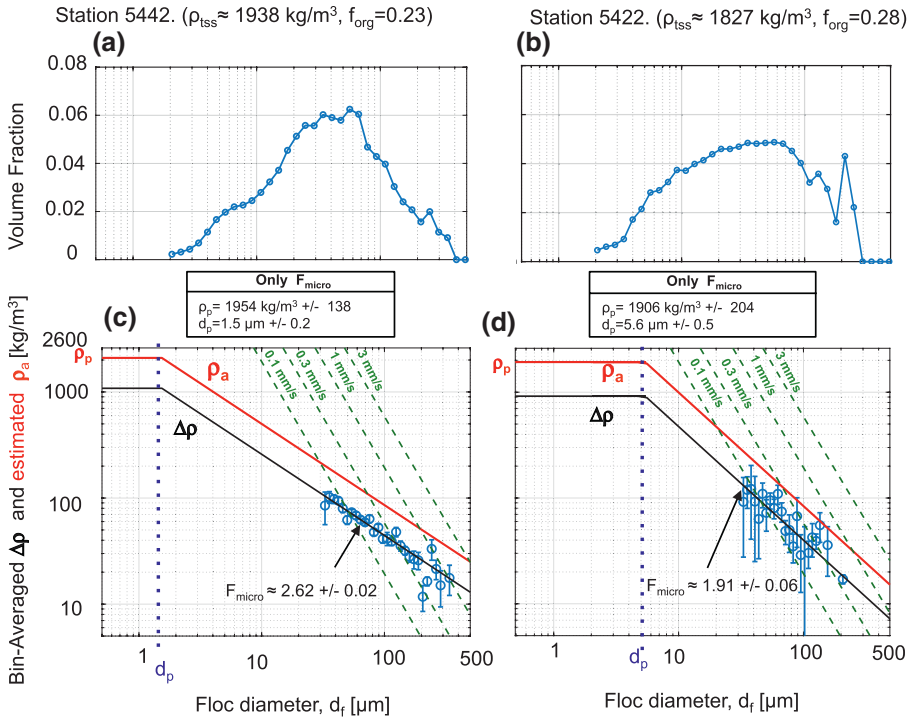

Figure 11. Example particle size distributions (a and b) and fractal characteristics (c and d) for two individual stations. Plots of bin-averaged $\Delta\rho$ versus d_f used 30 bins. Lines and symbols are as described in the caption of Figure 10.

4.3. Controls on Fractal Properties Inferred From Nonpooled Samples

The approach outlined in Figure 4 was also applied individually to all 65 samples to (1) further evaluate the use of fractal models to describe near-surface estuarine flocs and (2) further explore environmental controls on their fractal characteristics. However, this was not without some challenges, particularly in terms of data quality associated with lower concentration observations. The number of particles successfully tracked by the PICS at each individual station ranged from ~40 to 8,000. Naturally, the number of particles tracked by the PICS at each station was positively correlated to TSS (see Figure 9). Because individual stations had considerably fewer particles, $\Delta\rho$ for each station was bin averaged over 10-, 20-, and 30-size class bins rather than 75. Figure 11 shows the results from two example stations binned over 30-size class bins. The lower number of tracked particles at individual stations resulted in more noise in bin-averaged $\Delta\rho$, especially at large floc-size bins. On average, only 10% of the particles tracked were larger than 100 μm, and less than 1% of particles were larger than 200 μm. A majority of the individual stations did not have a large enough sample size at larger sizes to detect more than one fractal population (Figure 11). Because pooled samples suggest little disagreement for primary particle properties based on one fractal fit versus two fractal fits (Figure 10), and the large majority of the particle mass as well as individual particle observations are attributed to particles smaller than 100 μm, individual stations were fit with only one fractal group (F_{micro}) from 40 to 100 μm.

A total of 19 of the 65 samples could not be fit with a realistic fractal model from PICS observations because they showed a prohibitively high degree of scatter in $\Delta\rho$ versus d_f, and/or produced an unrealistic best-fit value for F. A realistic F_{micro} was defined such that the average best-fit value for $F_{40\text{–}100\ \mu\text{m}}$ for 10, 20, and 30 bin sets gave (1) $1 < F_{\text{micro}} < 3$ and (2) a standard error for F_{micro} that was less than 0.2. The remaining values for F_{micro} from individual stations ranged from 1.57 to 2.86, with an average F_{micro} of 2.36 ± 0.27. Despite this wide range, PICS fractal dimensions were generally consistent with fractal dimensions observed in other estuarine environments (Dyer & Manning, 1999; Sanford et al., 2005; Smith & Friedrichs, 2011; Winterwerp & van Kesteren, 2004).

For the remaining samples, primary particle properties were determined following the approach displayed in Figures 4 and 11, with the following additional quality control criteria applied to the best-fit results for ρ_p

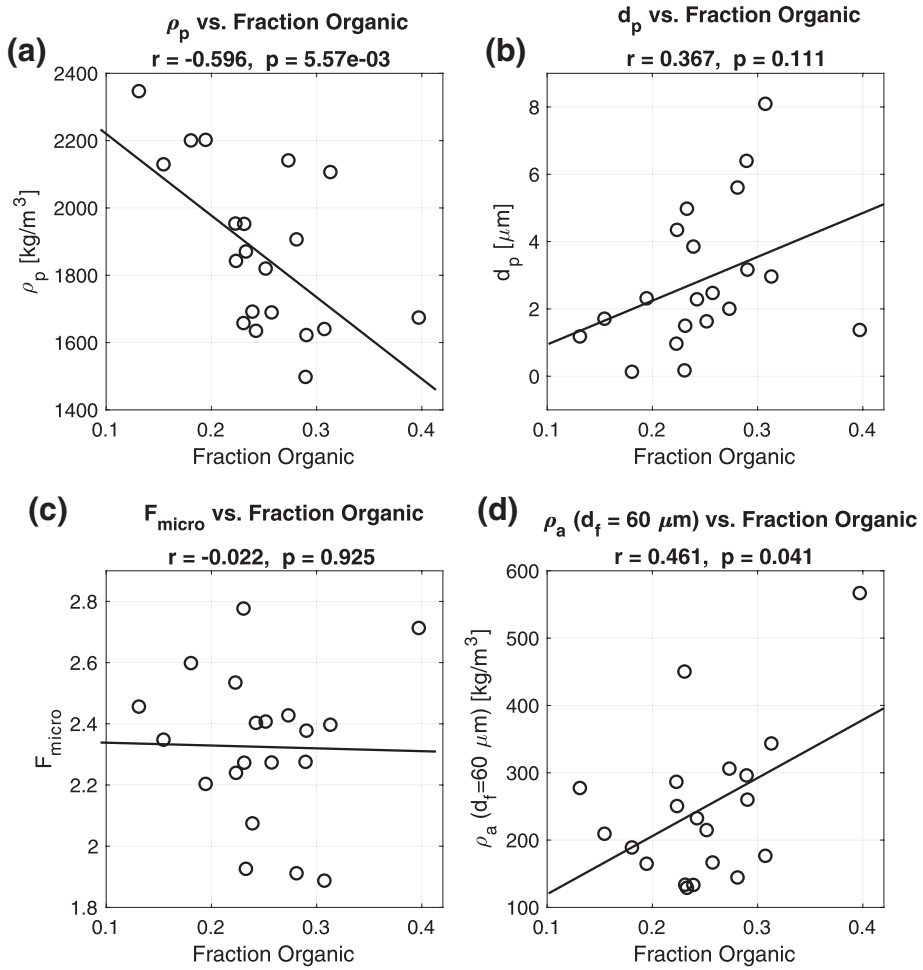

Figure 12. Regressions of fractal properties against f_{org} among the 20 samples, which individually passed quality control criteria for reasonable fractal fits. (a) ρ_p, (b) d_p, (c) F_{micro}, (d) ρ_{a_60mm}. Correlations (r), p-values (p), and best-fit lines are also displayed.

and d_p: (1) best-fit ρ_p was required to be within the realistic range of $1{,}200 < \rho_p < 2{,}500$ kg/m^3. This range was determined by calculating the ρ_{tss} using Equation 10 for the observed values of f_{org} over the range of possible ρ_{inorg} (2,600–2,800 kg/m^3) and ρ_{org} (700–1,600 kg/m^3) for the York (Maa & Kim, 2002; Mehta, 2014; Tyson, 1995; Wakeham & Canuel, 2016); (2) best-fit d_p was limited by realistic ranges suggested by the literature, such that $0.1 < d_p < 10$ μm (Fettweis, 2008; Mehta, 2014; Winterwerp, 1998); and (3) ρ_{org} calculated from Equation 10, using estimated ρ_p and observed f_{org}, was constrained to be within the realistic ranges suggested by the literature of $700 < \rho_{org} < 1{,}600$ kg/m^3 for the system. Based on the criteria listed above (including those in the previous paragraph), fractal models were "confidently" fit to 20 individual samples, that is, 31% of the original 65. These 20 samples had acceptably reliable derived values for F_{micro}, ρ_p, and d_p. They also reasonably represented the overall range in bulk variables seen in all 65 individual samples (see symbols filled with red stars in Figures 6 and 7).

For these 20 individual samples, the relationships between f_{org} and the variables ρ_{tss}, ρ_p, d_p, F_{micro}, ρ_a, and $\Delta\rho$ were found to be largely consistent with the patterns previously seen for the two pooled end-members. The strongest relationships were between f_{org} and ρ_p (Figure 12a) and, equivalently via Equation 10, between ρ_{tss} and ρ_p (Figure 13). The nearly 1:1 relationship between ρ_{tss} and ρ_p (also seen for the end-members) suggests that ρ_{tss} determined by water sampling is a reasonable estimate ρ_p for flocs that behave fractally. In fact, if Equations 4 and 5 held exactly for all particles in a suspension, one would find that ρ_{tss} would exactly equal ρ_p. For the 20 individual samples, a tendency ($p \approx 0.1$) was observed for d_p to increase with f_{org} (Figure 12b), which was consistent with the end-member results (Figure 10). A significant relationship was not seen

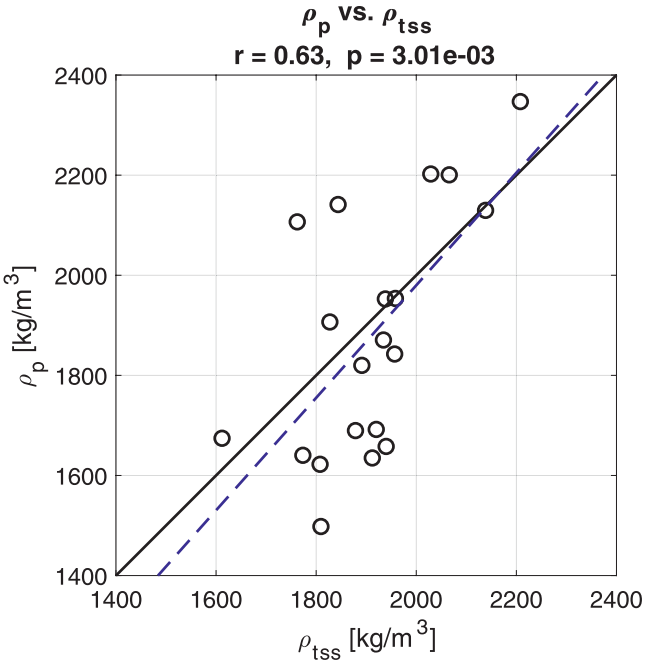

Figure 13. Primary particle density (ρ_p) for the 20 samples which individually passed quality control criteria for reasonable fractal fits plotted versus bulk dry particle density determined from pump sampling (ρ_{tss}). Both the best-fit relationship (blue dashed line) and the 1:1 relationship (solid black line) are shown.

between f_{org} and F_{micro} (Figure 12c) or between f_{org} and $\Delta\rho_{60\mu m}$, but $\rho_{a\_60\mu m}$ was seen to significantly increase with f_{org} (Figure 12d), again all consistent with the pooled end-members.

No correlations between TSS and the above variables for the 20 individual samples were significant. In all but one case, they were weaker than the correlations of the variables with f_{org}. (The exception was F_{micro}, for which $r = 0.034$ for TSS, compared to $r = -0.022$ for f_{org}.) The fact that TSS tended to be associated with weaker correlations than those associated with f_{org} for ρ_p, d_p, and $\rho_{a\_60\mu m}$ suggests that in this system, f_{org} is a stronger control on fractal floc properties than is TSS. The small degree of correlation that does exist between TSS and these variables may be present largely because of the strong inverse correlation between TSS and f_{org}, rather than the direct effects of TSS.

5. Discussion

5.1. Insights on Parameterization of F, d_p, and ρ_p in Fractal Approximations

This paper collected sufficient information utilizing simultaneous, in situ video settling, LISST, and sampling, such that is was possible to solve ρ_p, d_p, and F, simultaneously for individual samples without assuming that any of these three variables were constant across the samples. The methods applied here were built upon the approach of past authors who integrated a fractal model across observed volume concentrations as in Equations 5 and 6 (Bowers et al., 2017; Braithwaite et al., 2010; Chapalain et al., 2018; Ganju et al., 2007), but with the added constraint that here, F_{micro} was measured directly by the PICS. Others who have utilized Equations 5 and 6 in the past to solve for fractal properties have typically assumed constant values for ρ_p and d_p and matched the PSD to bulk ρ_a by letting F vary (e.g., Bowers et al., 2017; Braithwaite et al, 2010; Chapalain et al., 2018; Ganju et al., 2007). As a result, Chapalain et al. (2018) found F to systematically increase as organic content increased, although systematic changes in fractal variables might have been assigned to changes in d_p or ρ_p if they were allowed to vary. In this study, by allowing ρ_p, d_p, and F all to vary, we found that as f_{org} increased, d_p increased and ρ_p decreased, while F did not uniformly change. Given that this study found systematic trends in d_p and ρ_p, but not in F, future studies would be advised not to assume d_p and ρ_p to be constants while freely varying F. This is especially true given that sensitivity tests have shown that fractal fits and predicted sediment velocities are particularly sensitive to changes in d_p (Chapalain et al., 2018; Khelifa & Hill, 2006; Many et al., 2019; Verney et al., 2011).

5.2. Applicability of Simple Fractal Models

One of the unique aspects of this study was that the additional independent measure of F_{micro} from the PICS allowed us to identify how often a simple fractal model was justified. In fact, out of 65 independent samples, only 20 were individually found to confidently fit a simple fractal model without producing unrealistic or poorly constrained values for F, ρ_p, and/or d_p. In all the studies listed in the previous paragraph, a simple fractal model was assumed to apply, and fractal properties were solved without the additional degrees of freedom needed to test whether individual samples fit the specific fractal model. The inability to confidently fit a simple model for some of the samples collected in this study was likely due to instrument noise and/or small sample sizes. However, a notable fraction of cases that had relatively high TSS also failed to fit the simple fractal model, despite having thousands of tracked particles per sample (see high TSS cases without red stars in Figure 6). It is possible that non-fractal particles were commonly present, such as fecal pellets (G. M. Cartwright et al., 2011) or relatively large plankton or non-fractal detritus. It is also possible that the presence of organic material impacted individual floc structure and shapes, which would also cause deviation from a single, simple fractal model based on a Stokes or Stokes-like approximation (Dietrich, 1982;

Nguyen et al., 2020; Tang & Maggi, 2016). Other expressions for w_s, which better account for hydrodynamic drag on complex aggregates (e.g., Maggi, 2013), may be more appropriate for these flocs. Alternatively, perhaps two or more fractal populations were mixed together, each with distinct d_p, ρ_p, and/or F; or perhaps the F observed by the PICS in the microfloc range could not be justifiably extrapolated back to the primary particles. (Note that the somewhat more complex, variable F model of Khelifa and Hill (2006) was also applied to this study's data (not shown), but with no increase in the number of successful fits.) Given the minority of individual cases that could be confidently fit to the straightforward model used here, future studies would be well served to be more cautious in applying simple LISST-based fractal analysis, such as application of Equations 5 and 6 with imposed d_p and ρ_p, without the validity constraints provided by a video settling tube or other additional independent observations.

5.3. Validation of Simple Fractal Models With Independent Water Samples

Fractal models are built on the assumption that flocs are constructed from smaller solid components with the same composition, such that the bulk dry composition of flocs must be the same as the bulk dry composition of their primary particles. This means that if a fractal model holds, ρ_{tss} should be equal to ρ_p (Markussen & Andersen, 2013). Nonetheless, several studies of fractal particles properties in coastal and estuarine environments have assumed $\rho_p \approx$ 2,600–2,800, that is, equal to pure mineral matter (Chapalain et al., 2018; Fettweis, 2008; Hurley et al., 2016; Khelifa & Hill, 2006; Many et al., 2019; Sanford et al., 2005). Even when a lower value for ρ_p is chosen to account for a significant f_{org} (Bowers et al., 2017; Braithwaite et al., 2010), it is still treated as a constant within a given study. In contrast, in this study, the near 1:1 relationship between ρ_{tss} from the pump samples and modeled ρ_p (Figure 13) was noteworthy as well as consistent with previous analysis of sediments in the York River. Maa and Kim (2002) found that the inorganic material in the system is predominately illite clays ($\sim$ 75%), which has an average density of 2,750 kg/m^3 (Mehta, 2014). Typical particulate organic matter in the middle and lower York is detritus and exudates originally derived from plankton and bacteria; while the upper York particulate organic matter additionally includes marsh plant detritus (Countway et al., 2007; McCallister et al., 2006). The organic compounds associated with these sources (i.e., exopolymers, lipids, amino acids, etc.) span a range of densities centered around ~1,000 kg/m^3 (Maggi & Tang, 2015; Malpezzi et al., 2013; Tyson, 1995). Together, f_{org} x 1,000 kg/m^3 + (1 − f_{org}) x 2,750 kg/m^3 yielded the values in Figure 13. Thus, a simple consistency check for future applications of fractal models is to confirm that ρ_p used in fitting to floc observations is consistent with ρ_{tss} from water sampling.

5.4. Organics May Fill Spaces and Displace Water Within Flocs, Increasing Both d_p and ρ_a

This study found that as organic content increased (and ρ_p decreased), d_p tended to increase. Maggi (2013) found a similar pattern based on a survey of experimental results from the literature. Specifically, Maggi (2013) found mean d_p ($<d_p>$) ≈ 0.5 μm for $f_{org} < 0.2$, $<d_p> \approx$ 2.4 μm for $0.2 \le f_{org} \le 0.4$, and $<d_p> \approx$ 4.3 μm for $f_{org} > 0.4$. Illite, which is the most common mineral in York River sediments, has a typical diameter of about 0.1 μm for individual plates (Mehta, 2014), which is about the size of the smallest values determined for d_p in Figure 12b. This suggests that, except for the very smallest primary particles present in the York, primary particles in this study are likely tightly bound aggregates of relatively larger organic matter fragments combined with smaller clay plates. As f_{org} increases, the results suggest that organic matter is more likely to completely "fill in" the framework of progressively larger inorganic floccules, leading to a larger d_p. Because ρ_{org} is close to the density of water, having more organic matter within small flocs, including microflocs, would not have notably changed $\Delta\rho$. However, ρ_a for microflocs, which is based on total dry mass, including low density organic matter, would increase, because a portion of the space containing only water in inorganic flocs would now contain organics, which would be caught on glass fiber filters. This could explain why bulk ρ_a was observed to increase with f_{org} in Figure 6g, and $\rho_{a\_60\mu m}$ was observed to increase with f_{org} in Figure 12d. This would also explain why higher f_{org} cases tended to fall above the best-fit line relating bulk ρ_a to d_{50v} in Figure 7, while lower f_{org} cases tended to fall below the line.

Previous research in the York (G. M. Cartwright et al., 2013; Fugate & Friedrichs, 2002), Chesapeake Bay (Sanford & Halka, 1993), and other systems (Jago & Jones, 1998) have observed a background concentration of continuously suspended particles, typically in the range of 5–10 mg/l, which varies very little in either

time or space. It is debated whether these background concentrations are composed of individual particles or small, tightly bound aggregates. Based on the PSDs documented here, it is suggested that this population exists as small aggregated material of the order of 5–10 μm in size, which is close to the size of d_p estimated here for organic-rich flocs.

5.5. Observed Change in *F* at the Transition to Macroflocs

When pooling multiple samples together to reduce scatter, a "kink" or breakpoint in fractal dimension was seen at the transition from microflocs to macroflocs, corresponding to a settling velocity (w_s) of ~1 mm/s (Figures 8 and 10). Kinks or bends in best-fits have been observed before, which has led to the concept that size-varying fractal dimensions may be more appropriate for PSDs spanning orders of magnitude of floc size (Khelifa & Hill, 2006; Kumar et al., 2010; Maggi, 2007, 2013). Different fractal dimensions indicate that some aspect of the self-similar structure of flocs has changed. Systematic changes in component particles could cause a deviation away from a single fractal dimension for a given population (Chapalain et al., 2018; Khelifa & Hill, 2006). As flocs become larger, it is possible that they are preferentially being built from a distinct subset of the available smaller components, such that characteristic floc composition is not independent of floc size. Or physics, rather than composition, may favor a change in characteristic F with size. Large, moderately dense flocs may produce high enough settling velocities such that their downward velocity sheds turbulent eddies which, in turn, produce stresses that break the flocs apart. Previous authors have found that turbulent eddies capable of tearing apart flocs begin at velocities of ~1 mm/s (Adler, 1979; Hill et al., 1998). Thus, very weak flocs would tend to break up if their size and density led to $w_s > \sim 1$ mm/s. In fact, the best-fit F_{macro} in Figure 10d (green dashed line) corresponds very closely with the line for $w_s = 1$ mm/s, suggesting that the larger, high f_{org} flocs observed in the York were quite weak. Although a (less dramatic) breakpoint is also seen for low f_{org} flocs in Figure 10c, the resulting macroflocs have $w_s > 1$ mm/s, which implies that low f_{org} flocs tended to be relatively stronger in comparison. This finding is opposite relative to the common wisdom regarding the usual role of organic matter in enhancing the strength of macroflocs (Cross et al., 2013; Fettweis & Baeye, 2015; Malpezzi et al., 2013; Sanford et al., 2005; Uncles et al., 2010). However, a lower f_{org} was also correlated with a higher U, which suggests that a higher U may be suspending denser, stronger macroflocs into surface waters. However, the present data set was limited in terms of the quantity of macroflocs observed, and studies that include more macroflocs together with simultaneously observed microflocs are warranted to further investigate controls on changing F with aggregate size.

5.6. Additional Limitations

It is important to consider the systematic limitations of the PICS that may have influenced the observations of d_f and $\Delta\rho$, specifically issues resolving smaller particle sizes and sampling stations that had very low total mass concentrations. Smaller flocs ($d_f < 80$ μm) accounted for a majority contribution to the surface suspensions (Figure 5), and at most stations, TSS concentrations were less than 25 mg/L (Figure 6). Both of these properties limit the number of particles available for the PICS to successfully track. In addition, post-analysis revealed that the laser intensity or lighting illumination setting used to collect these samples was less than ideal for the environment and should have been increased. The low illumination made it more difficult to identify and track smaller flocs, even for those within the PICS resolution range. Despite PIV analysis, the sampling conditions still resulted in large scatter for the observations. Characterizing background fluid velocities was also more challenging for poorly illuminated samples with low concentrations (Smith & Friedrichs, 2015). An appropriate fractal model may not have been determined in some cases because the suspensions were not fully resolved, or not enough observations were available to average out sampling noise. Finally, the approach assumed PICS fractal models extended to flocs significantly smaller than the lower resolutions limit of the PICS ($d_f \approx 30$ μm), which may not be realistic. Future work will involve modifying the current PICS system to include a dual microscopy-camera based system that will be able to measure particle size, settling velocity, and density over a more complete range of floc sizes, including $d_f \approx 5$–2,000 μm, in order to better constrain the fractal properties of smaller flocs.

It should also be considered as to whether estimates of TSS from PSDs and TSS observed from pump samples are based on compatible particle size ranges. If the size range of particles contributing to pumped TSS is greater than the range contributing to ΣVC_i, ρ_a will be overestimated (Bowers et al., 2009). Overestimating ρ_a propagates to an underestimate of ρ_p (Equation 3) and an overestimate of d_p (Equation 5). The nominal pore size of the glass fiber filters used here is 0.7 μm, so all particles larger than this can be caught on the filter and contribute to TSS. Merging the PICS and LISST extended the size range of VC_i up to 1,000 μm. The vast majority of PSDs dropped off sharply well before 1,000 μm (Figure 5), and very few large flocs were identified by the PICS (less than 1% with $d_f > 200$ μm). Data suggest that particles with diameters larger than the combined PSD range did not contribute significantly to TSS. As for particles smaller than the LISST-100 Type C resolvable range ($d_f < 2.5$ μm), simultaneous sampling with a co-located LISST-100x Type B (range 1.25–250 μm) determined that contributions from particles <2.5 μm were likely negligible and were not a notable source of error.

6. Conclusions and Recommended Future Work

- By combining LISST, video settling, and pump sampling, this study developed a new method to simultaneously solve for fractal dimension (F), primary particle diameter (d_p), and density (ρ_p). The method's key components are (1) fitting a simple fractal model to observations of excess density ($\Delta\rho$) as a function of floc diameter (d_f) and (2) ensuring the integrated PSD are consistent with measurements of bulk floc apparent density (ρ_{a_bulk}). Applications of this technique will avoid the need to unrealistically assume constant values for d_p or ρ_p a priori, thus reducing the reliance on unconstrained, highly variable values for F, and better identify when simple fractal models do or do not apply
- Even with the promise of the above method, flocs are still difficult to measure with in situ video settling columns due to high levels of noise. This is especially true in estuarine surface waters, where floc concentrations are low, particles are small, a stable in situ settling platform is difficult to maintain, and high organic content may reduce optical contrast. Future sampling should average over longer or more consecutive sampling periods and utilize more advanced contrast correction algorithms
- When large numbers of observations were pooled, $\Delta\rho$ as a function of d_f was found to be strongly fractal, with a well-constrained best-fit microfloc F for a given set of pooled samples. Rather than a continual reduction in F with greater d_f, F was observed to decrease rather suddenly via a breakpoint in $\Delta\rho$ versus d_f near the transition from microflocs to macroflocs, with a sharper breakpoint present for a higher f_{org}. Future work is needed to confirm whether or not the kink is related to the presence of additional turbulent stresses induced by settling for $w_s \geq \sim 1$ mm/s
- Application of the above methods showed the bulk fraction of organic matter (f_{org}) to be well correlated with both median floc size by volume (d_{50v}) and bulk floc apparent density (ρ_{a_bulk}). These floc properties were more strongly correlated to f_{org} than to TSS concentration. As f_{org} increased, the following quantities increased: primary particle size, ρ_{a_bulk}, and representative apparent density of 60 μm microflocs, whereas the following decreased: primary particle density, primary particle density inferred from TSS composition, d_{50v}, TSS, and representative excess density of 200 μm macroflocs. In contrast, fractal dimensions fit from 40 to 100 μm and representative excess density of 60 μm microflocs did not systematically increase or decrease in response to f_{org}
- Results suggest that in the York, (1) primary particles are tightly bound aggregates of relatively larger organic matter fragments combined with smaller clay plates and (2) as f_{org} increases, organic matter is more likely to completely "fill in" the framework of progressively larger inorganic floccules, leading to larger primary aggregate size. Because the density of organic solids is close to the density of water, having more organic matter within small flocs, including microflocs, does not notably change excess density ($\Delta\rho$). In contrast, having more organic matter does increase apparent density (ρ_a) for microflocs, which is based on the total dry mass. This is because a portion of the space containing only water in inorganic flocs now contains organics, which ends up caught on the filters used to calculate ρ_a
- Regardless of the fraction of organic matter at the sites sampled here, the majority of flocs by number, volume, and mass were always contained in microflocs and even smaller size classes rather than within macroflocs. When considering the full LISST–PICS merged PSD, only 4% of the dry mass in the average PSD was contained in macroflocs ($d_f > 150$ μm); similarly, <1% of particles tracked by the PICS had

$d_f > 200$ μm. Future work with video settling tubes should strive to include LISST to avoid undersampling small d_f

- The least constrained component of simple fractal models is d_p. Fractal dimension, F, can be directly measured by video settling tubes (although further decreases in pixel size are desired), and ρ_p can be constrained by filtering water samples. However, there are no established methods to directly measure d_p, in situ. Future work should develop methods to measure the size of primary particles (or tightly bound primary aggregates) directly, while being careful not to break them apart or alter their organic content
- Although this study focused on solely on the York, findings are still helpful in considering the relationships among fractal floc properties and organic solids fraction in other systems. Many of the resultant fractal properties seen in this set of observations were consistent with previous studies, in which samples were derived from a variety of locations (e.g., see Braithwaite et al., 2010; Chapalain et al., 2018; Khelifa & Hill, 2006; Maggi, 2013). However, this study purposely avoided high concentrations of living phytoplankton, and the notable, inverse spatial gradients in TSS and organic fraction seen here are not always the case. Future work applying the methods developed in this study to other estuarine systems will add to our understanding of floc dynamics encompassing more diverse mixtures of organic and inorganic solids

Data Availability Statement

Data used in this analysis are publicly available thru William & Mary's ScholarWorks (https://doi.org/10.25773/7gbc-6739).

Acknowledgments
The authors thank the VIMS Field operations group, notably Tim Gass and Wayne Reisner for field support. Marjy Friedrichs, Courtney Harris, Ken Moore, and Larry Sanford contributed advice and helped with early revisions to the manuscript. The authors also thank Frederico Maggi and a second anonymous reviewer for their constructive feedback. Funding for this research was provided by the National Science Foundation, Grants OCE-1061781 and OCE-1459708 and a Virginia Water Resource Research Center student grant. This article is contribution No. 3964 of the Virginia Institute of Marine Science, William & Mary.

References

Adler, P. M. (1979). A study of disaggregation effects in sedimentation. *AIChE Journal*, *25*, 487–493. https://doi.org/10.1002/aic.690250314

Agrawal, Y. C., & Pottsmith, H. C. (2000). Instruments for particle size and settling velocity observations in sediment transport. *Marine Geology*, *168*, 89–114. https://doi.org/10.1016/S0025-3227(00)00044-X

Agrawal, Y. C., Whitmire, A., Mikkelsen, O. A., & Pottsmith, H. C. (2008). Light scattering by random shaped particles and consequences on measuring suspended sediments by laser diffraction. *Journal of Geophysical Research*, *113*, C04023. https://doi.org/10.1029/2007JC004403

Andrews, S., Nover, D., & Schladow, S. G. (2010). Using laser diffraction data to obtain accurate particle size distributions: The role of particle composition. *Limnology and Oceanography: Methods*, *8*, 507–526. https://doi.org/10.4319/lom.2010.8.507

Babin, M., Morel, A., Fournier-Sicre, V., Fell, F., & Stramski, D. (2003). Light scattering properties of marine particles in coastal and open ocean waters as related to the particle mass concentration. *Limnology and Oceanography*, *48*, 843–859. https://doi.org/10.4319/lo.2003.48.2.0843

Bowers, D. G., Braithwaite, K. M., Nimmo-Smith, W. A. M., & Graham, G. W. (2009). Light scattering by particles suspended in the sea: The role of particle size and density. *Continental Shelf Research*, *29*, 1748–1755. https://doi.org/10.1016/j.csr.2009.06.004

Bowers, D. G., Braithwaite, K. M., Nimmo-Smith, W. A. M., & Graham, G. W. (2011). The optical efficiency of flocs in shelf seas and estuaries. *Estuarine, Coastal and Shelf Science*, *91*, 31–350. https://doi.org/10.1016/j.ecss.2010.10.019

Bowers, D. G., McKee, D., Jago, C. F., & Nimmo-Smith, W. A. M. (2017). The area to-mass ratio and fractal dimension of marine flocs. *Estuarine, Coastal and Shelf Science*, *189*, 224–234. https://doi.org/10.1016/j.ecss.2017.03.026

Braithwaite, K. M., Bowers, D. G., Nimmo Smith, W. A. M., Graham, G. W., Agrawal, Y. C., & Mikkelsen, O. A. (2010). Observations of particle density and scattering in the Tamar Estuary. *Marine Geology*, *277*, 1–10. https://doi.org/10.1016/j.margeo.2010.06.008

Cartwright, G. M., Friedrichs, C. T., & Sanford, L. P. (2011). In situ characterization of estuarine suspended sediment in the presence of muddy flocs and pellets. In P. Wang, J. D. Rosati, & T. M. Roberts (Eds.), *Coastal sediments 2011* (pp. 642–655). World Scientific. https://doi.org/10.1142/9789814355537_0049

Cartwright, G. M., Friedrichs, C. T., & Smith, S. J. (2013). A test of the ADV-based Reynolds-flux method for in situ estimation of sediment settling velocity in a muddy estuary. *Geo-Marine Letters*, *33*, 477–484. https://doi.org/10.1007/s00367-013-0340-4

Chapalain, M., Verney, R., Fettweis, M., Jacquet, M., Le Berre, D., & Hir, P. (2018). Investigating suspended particulate matter in coastal waters using the fractal theory. *Ocean Dynamics*, *69*, 59–81. https://doi.org/10.1007/s10236-018-1229-6

Countway, R. E., Canuel, E. A., & Dickhudt, R. M. (2007). Sources of particulate organic matter in surface waters of the York River, VA estuary. *Organic Geochemistry*, *38*, 365–279. https://doi.org/10.1016/j.orggeochem.2006.06.004

Cross, J., Nimmo-Smith, W. A. M., Torres, R., & Hosegood, P. J. (2013). Biological controls on resuspension and the relationship between particle size and the Kolmogorov length scale in a shallow coastal sea. *Marine Geology*, *343*, 29–38. https://doi.org/10.1016/j.margeo.2013.06.014

Dietrich, W. E. (1982). Settling velocity of natural particles. *Water Resources Research*, *18*, 1615–1626. https://doi.org/10.1029/WR018i006p01615

Dyer, K. R., Cornelise, J., Dearnaley, M. P., Fennessy, M. J., Jones, S. E., Kappenberg, J., et al.(1996). A comparison of in situ techniques for estuarine floc settling velocity measurements. *Journal of Sea Research*, *36*, 15–29. https://doi.org/10.1016/S1385-1101(96)90766-2

Dyer, K. R., & Manning, A. J. (1999). Observation of the size, settling velocity and effective density of flocs, and their fractal dimensions. *Journal of Sea Research*, *41*, 87–95. https://doi.org/10.1016/S1385-1101(98)00036-7

Fennessy, M. J., & Dyer, K. R. (1996). Floc population characteristics measured with INSSEV during the Elbe Estuary intercalibration experiment. *Journal of Sea Research*, *26*, 55–62. https://doi.org/10.1016/S1385-1101(96)90771-6

Fettweis, M. (2008). Uncertainty of excess density and settling velocity of mud flocs derived from in situ measurements. *Estuarine, Coastal and Shelf Science*, *78*, 426–436. https://doi.org/10.1016/j.ecss.2008.01.007

Fettweis, M., & Baeye, M. (2015). Seasonal variation in concentration, size, and settling velocity of muddy marine flocs in the benthic boundary layer. *Journal of Geophysical Research: Oceans*, *120*, 5648–5667. https://doi.org/10.1002/2014JC010644

Friedrichs, C. T. (2009). York river physical oceanography and sediment transport. In K. A. Moore, & W. G. Reay (Eds.), *A site profile of the Chesapeake Bay national estuarine research reserve, Virginia Journal of coastal research, SI* (Vol. 57, pp. 17–22) Coastal Education and Research Foundation. https://doi.org/10.2112/1551-5036-57.sp1.17

Friedrichs, C. T., Cartwright, G. M., & Dickhudt, P. J. (2008). Quantifying benthic exchange of fine sediment via continuous, noninvasive, measurements of settling velocity and bed erodibility. *Oceanography*, *21*(4), 168–172. https://doi.org/10.5670/oceanog.2008.14

Fugate, D. C., & Friedrichs, C. T. (2002). Determining concentration and fall velocity of estuarine particle populations using ADV, OBS, and LISST. *Continental Shelf Research*, *22*, 1867–1886. https://doi.org/10.1016/S0278-4343(02)00043-2

Fugate, D. C., & Friedrichs, C. T. (2003). Controls on suspended aggregate size in partially mixed estuaries. *Estuarine, Coastal and Shelf Science*, *58*, 389–404. https://doi.org/10.1016/S0272-7714(03)00107-0

Gallegos, C. L., Werdell, P. J., & McClain, C. R. (2011). Long-term changes in light scattering in Chesapeake Bay inferred from Secchi depth, light attenuation, and remote sensing measurements. *Journal of Geophysical Research*, *116*, C00H08. https://doi.org/10.1029/2011JC007160

Ganju, N. K., Schoellhamer, D. H., Murrell, M. C., Gartner, J. W., & Wright, S. A. (2007). Constancy of the relation between floc size and density in San Francisco Bay. In J. P.-Y. Maa, L. P. Sanford, & D. H. Schoellhamer (Eds.), *Estuarine and coastal fine sediments dynamics* (pp. 75–91). Amsterdam, the Netherlands: Elsevier Science B.V. http://www.worldcat.org/isbn/0444521631

Hill, P. S., Boss, E., Newgard, J. P., Law, B. A., & Milligan, T. G. (2011). Observations of the sensitivity of beam attenuation to particle size in a coastal bottom boundary layer. *Journal of Geophysical Research*, *116*, C02023. https://doi.org/10.1029/2010JC006539

Hill, P. S., Bowers, D. G., & Braithwaite, K. M. (2013). The effect of suspended particle composition on particle area-to-mass ratios in coastal waters. *Methods in Oceanography*, *7*, 95–109. https://doi.org/10.1016/j.mio.2014.02.003

Hill, P. S., Syvitski, J. P., Cowan, E. A., & Powell, R. D. (1998). In situ observations of floc settling velocities in Glacier Bay, Alaska. *Marine Geology*, *145*, 85–94. https://doi.org/10.1016/S0025-3227(97)00109-6

Hurley, A. J., Hill, P. S., Milligan, T. G., & Law, B. A. (2016). Optical methods for estimating apparent density for sediment in suspension. *Methods in Oceanography*, *17*, 153–168. https://doi.org/10.1016/j.mio.2016.09.001

Jago, C. F., & Jones, S. E. (1998). Observation and modelling of the dynamics of benthic fluff resuspended from a sandy bed in the southern Northern Sea. *Continental Shelf Research*, *18*, 1255–1282. https://doi.org/10.1016/S0278-4343(98)00043-0

Khelifa, A., & Hill, P. S. (2006). Models for effective density and settling velocity of flocs. *Journal of Hydraulic Research*, *44*, 390–401. https://doi.org/10.1080/00221686.2006.9521690

Kranenburg, C. (1994). The fractal structure of cohesive sediment aggregates. *Estuarine, Coastal and Shelf Science*, *29*, 451–460. https://doi.org/10.1016/S0272-7714(06)80002-8

Kumar, G. R., Strom, K. B., & Keyvani, A. (2010). Floc properties and settling velocity of San Jacinto estuary mud under variable shear and salinity conditions. *Continental Shelf Research*, *30*, 2067–2081. https://doi.org/10.1016/j.csr.2010.10.006

Lee, B. J., Fettweis, M., Tooman, E., & Molz, F. J. (2012). Multimoldality of particle size distribution of cohesive particle matters in a coastal zone. *Journal of Geophysical Research*, *117*, C03014. https://doi.org/10.1029/2011JC007552

Lee, B. J., Toorman, E., & Fettweis, M. (2014). Multimodal particle size distributions of fine-grained sediments: mathematical modeling and field investigation. *Ocean Dynamics*, *64*, 429–441. https://doi.org/10.1007/s10236-014-0692-y

Maa, J. P. Y., & Kim, S. C. (2002). A constant erosion rate for fine sediment in the York River, Virginia. *Environmental Fluid Mechanics*, *1*, 345–360. https://doi.org/10.1023/A:1015799926777

Maggi, F. (2007). Variable fractal dimension: A major control for floc structure and flocculation kinematics of suspended cohesive sediment. *Journal of Geophysical Research*, *112*, (C7). http://dx.doi.org/10.1029/2006jc003951

Maggi, F. (2013). The settling velocity of mineral, biomineral, and biological particles and aggregates in water. *Journal of Geophysical Research Oceans*, *118*, 2118–2132. https://doi.org/10.1002/jgrc.20086

Maggi, F., & Tang, F. H. M. (2015). Analysis of the effect of organic matter content on the architecture and sinking of sediment aggregates. *Marine Geology*, *363*, 102–111. https://doi.org/10.1016/j.margeo.2015.01.017

Malpezzi, M. A., Sanford, L. P., & Crump, B. C. (2013). Abundance and distribution of transparent exopolymer particles in the estuarine turbidity maximum of Chesapeake Bay. *Marine Ecology Progress Series*, *486*, 23–35. https://doi.org/10.3354/meps10362

Many, G., Durrieu de Madron, X., Verney, R., Bourrin, F., Renosh, P. R., Jourdin, F., & Gangloff, A. (2019). Geometry, fractal dimension and settling velocity of flocs during flooding conditions in the Rhône ROFI. Estuarine. *Coastal and Shelf Science*, *219*, 1–13. https://doi.org/10.1016/j.ecss.2019.01.017

Markussen, T. N., & Andersen, T. J. (2013). A simple method for calculating in situ floc settling velocities based on effective density functions. *Marine Geology*, *344*, 10–18. https://doi.org/10.1016/j.margeo.2013.07.002

McCallister, S. L., Bauer, J. E., Ducklow, H. W., & Canuel, E. A. (2006). Sources of estuarine dissolved and particulate organic matter: A multi-tracer approach. *Organic Geochemistry*, *37*, 454–468. https://doi.org/10.1016/j.orggeochem.2005.12.005

Mehta, A. J. (2014). An introduction to hydraulics of fine sediment transport. Advanced series on ocean engineering (Vol. 38). World Scientific. http://www.worldcat.org/isbn/9814449482

Mikkelsen, O. A., Hill, P. S., & Milligan, T. G. (2006). Single-grain, microfloc and macrofloc volume variations observed with a LISST-100 and a digital floc camera. *Journal of Sea Research*, *55*, 87–102. https://doi.org/10.1016/j.seares.2005.09.003

Mikkelsen, O. A., Hill, P. S., Milligan, T. G., & Chant, R. J. (2005). In situ particle size distributions and volume concentrations from a LISST-100 laser particle sizer and a digital floc camera. *Continental Shelf Research*, *25*, 1959–1978. https://doi.org/10.1016/j.csr.2005.07.001

Mikkelsen, O. A., Milligan, T. G., Hill, P. S., & Moffatt, D. (2004). INSSECT—an instrumented platform for investigating floc properties close to the seabed. *Limnology and Oceanography Methods*, *2*, 226–236. https://doi.org/10.4319/lom.2004.2.226

Mikkelsen, O. A., & Pejrup, M. (2001). The use of a LISST-100 in-situ laser particle sizer for in situ estimates of floc size, density and settling velocity. *Geo-Marine Letters*, *20*, 187–195. https://doi.org/10.1007/s003670100064

Milligan, T. G., & Hill, P. S. (1998). A laboratory assessment of the relative importance of turbulence, particle composition, and concentration in limiting maximal floc size and settling behaviour. *Journal of Sea Research*, *39*, 227–241. https://doi.org/10.1016/S1385-1101(97)00062-2

Moore, K. A., Wetzel, R. L., & Orth, R. J. (1997). Seasonal pulses of turbidity and their relations to eelgrass (Zostera marina L.) survival in an estuary. *Journal of Experimental Marine Biology and Ecology*, *215*, 115–134. https://doi.org/10.1016/S0022-0981(96)02774-8

Murphy, R. R., Perry, E., Harcum, J., & Keisman, J. (2019). A generalized additive model approach to evaluating water quality: Chesapeake Bay case study. *Environmental Modelling & Software*, *118*, 1–13. https://doi.org/10.1016/j.envsoft.2019.03.027

Nguyen, T. H., Tang, F. H. M., & Maggi, F. (2020). Sinking of microbial-associated microplastics in natural waters. *PloS One*, *15*(2), e0228209. https://doi.org/10.1371/journal.pone.0228209

Reay, W. (2009). Water quality within the York River Estuary. In K. A. Moore, & W. G. Reay (Eds.), A site profile of the Chesapeake Bay national estuarine research reserve, Virginia Journal of coastal research, SI. (Vol. 57, pp. 23–39). Coastal Education and Research Foundation. https://doi.org/10.2112/1551-5036-57.sp1.23

Reynolds, R. A., Stramski, D., Wright, V. M., & Woźniak, S. B. (2010). Measurements and characterization of particle size distributions in coastal waters. *Journal of Geophysical Research*, *115*, C08024. https://doi.org/10.1029/2009JC005930

Sanford, L. P., Dickhudt, P. J., Rubiano-Gomez, L., Yates, M., Suttles, S. E., Friedrichs, C. T., et al. (2005). Variability of suspended particle concentrations, sizes, and settling velocities in the Chesapeake Bay turbidity maximum. In I. G. Droppo, G. G. Leppard, S. N. Liss, & T. G. Milligan (Eds.), *Flocculation in natural and Engineered environmental systems* (pp. 211–236). CRC Press. https://doi.org/10.1201/9780203485330

Sanford, L. P., & Halka, J. P. (1993). Assessing the paradigm of mutually exclusive erosion and deposition of mud, with examples from upper Chesapeake Bay. *Marine Geology*, *114*, 37–57. https://doi.org/10.1016/0025-3227(93)90038-W

Schaffner, L. C., Hinchey, E. K., Dellapenna, T. M., Friedrichs, C. T., Neubauer, M. E., Smith, M. E., & Kuehl, S. A. (2001). Physical energy regimes, sea-bed dynamics and organism-sediment interactions along an estuarine gradient. In J. Y. Aller, S. A. Woodin, & R. C. Aller (Eds.), *Organism–sediment interactions* (pp. 159–179). Columbia, SC: Univ ersity of South Carolina Press. http://www.worldcat.org/isbn/1570034311

Sin, Y., Wetzel, R. L., & Anderson, I. C. (1999). Spatial and Temporal Characteristics of Nutrient and Phytoplankton Dynamics in the York River Estuary, Virginia: Analyses of Long-Term Data. *Estuaries*, *22* (2), 260–275. http://dx.doi.org/10.2307/1352982

Smith, S. J., & Friedrichs, C. T. (2011). Size and settling velocities of cohesive flocs and suspended sediment aggregates in a trailing suction hopper dredge plume. *Continental Shelf Research*, *31*(10S), S50–S63. https://doi.org/10.1016/j.csr.2010.04.002

Smith, S. J., & Friedrichs, C. T. (2015). Image processing methods for in situ estimations of cohesive sediment floc size, settling velocity, and density. *Limnology and Oceanography Methods*, *13*, 250–264. https://doi.org/10.1002/lom3.10022

Son, M., & Hsu, T. J. (2011). The effects of flocculation and bed erodibility on modeling cohesive sediment resuspension. *Journal of Geophysical Research*, *116*, C03021. https://doi.org/10.1029/2010JC006352

Soulsby, R. L. (1997). *Dynamics of marine sands*. Thomas Telford http://www.worldcat.org/isbn/072772584X

Tang, F. H. M., & Maggi, F. (2016). A mesocosm experiment of suspended particulate matter dynamics in nutrient- and biomass-affected waters. *Water Research*, *89*, 76–86. https://doi.org/10.1016/j.watres.2015.11.033

Tyson, R., , & (1995). *Sedimentary organic matter: Organic facies and palynofacies*. London, UK: Chapman and Hall. http://www.worldcat.org/isbn/041236350X

Uncles, R. J., Bale, A. J., Stephens, P. E., Frickers, P. E., & Harris, C. (2010). Observations of floc sizes in a muddy Estuary. *Estuarine, Coastal and Shelf Science*, *87*, 186–196. https://doi.org/10.1016/j.ecss.2009.12.018

USEPA (1983). *Methods for chemical analysis of water and wastes. Methods No, 160*. USEPA.

Van Leussen, W., & Cornelisse, J. M. (1993). The determination of the sizes and settling velocities of estuarine flocs by an underwater video system. *Netherlands Journal of Sea Research*, *31*, 231–241. https://doi.org/10.1016/0077-7579(93)90024-M

Verney, R., Lafite, R., Claude Brun-Cottan, J., & Le Hir, P. (2011). Behaviour of a floc population during a tidal cycle: Laboratory experiments and numerical modelling. *Continental Shelf Research*, *31*(S10), S64–S83. https://doi.org/10.1016/j.csr.2010.02.005

Wakeham, S. G., & Canuel, E. A. (2016). The nature of organic carbon in density-fractioned sediments in the Sacramento-San Joaquin River Delta (California). *Biogeosciences*, *13*, 567–582. https://doi.org/10.5194/bg-13-567-2016

Winterwerp, J. C. (1998). A simple model for turbulence induced flocculation of cohesive sediment. *Journal of Hydraulic Research*, *36*, 309–326. https://doi.org/10.1080/00221689809498621

Winterwerp, J. C. (2002). On the flocculation and settling velocity of estuarine mud. *Continental Shelf Research*, *22*, 1339–1360. https://doi.org/10.1016/S0278-4343(02)00010-9

Winterwerp, J. C., & van Kesteren, W. G. M. (2004). Introduction to the physics of cohesive sediment in the marine environment, developments in sedimentology Series. Elsevier. http://www.worldcat.org/isbn/0444515534